Title
Therapeutic Nanotechnology and Immunoengineering for Cellular Therapy in Autoimmune Diabetes and Cancer

Author
Chang, Ryan

Publication Date
2017

Peer reviewed|Thesis/dissertation

Therapeutic Nanotechnology and Immunoengineering for Cellular Therapy in Autoimmune Diabetes and Cancer

by

Ryan Chang

DISSERTATION

Submitted in partial satisfaction of the requirements for the degree

DOCTOR OF PHILOSOPHY

in Bioengineering

in the

GRADUATE DIVISION

of the

UNIVERSITY OF CALIFORNIA, SAN FRANCISCO

AND

UNIVERSITY OF CALIFORNIA, BERKELEY

[redacted]

ACKNOWLEDGMENTS

This research project was inspired and motivated by all the patients and their families affected by diabetes or cancer. It is my hope that the science and technologies developed during my graduate training may someday contribute to alleviating pain and improving quality of life for patients. The project would not have been possible without the support of many people. I would like to express my deepest gratitude to my research supervisor, Prof. Tejal Desai and collaborative research advisors Prof. Qizhi Tang, Prof. Matthias Hebrok, and Prof. Lawrence Fong, for providing me with the resource, support, and mentorship at every stage of my graduate scientific training.

I am extraordinarily grateful and proud to be have the opportunity to work with an interdisciplinary team of stellar scientists including bioengineers, transplant immunologists, stem cell biologists, immuno-oncologists and physician scientists. Prof. Desai offered me the ideal environment to innovate and iterate rapidly with high risk research ideas in a translational setting. I also want to thank Prof. Tang for being tremendously invested and instilling great scientific rigor throughout my training. Thank you to Prof. Matthias Hebrok for believing in bioengineered devices for stem cell transplants and being a strong advocate for our research. Lastly, I want to thank Prof. Lawrence Fong for being a wonderful attending physician mentor to me in both the UCSF genitourinary medical oncology practice and the UCSF

Institute for Cancer Immunotherapy for his clinical teachings and for giving me the opportunity to participate in the care for cancer patients.

I would also like to acknowledge the UCSF Medical Scientist Training Program, Juvenile Diabetes Research Foundation, and UCSF Program for Breakthrough Biomedical Research for grant funding and stipend support. Special thanks also to my post doc colleagues Gaetano Faleo, Holger Russ, Audrey Parent, Steven Wisel, Daniel Bernard for offering your assistance and guidance to further this project.

I am grateful to my close colleagues and friends Long Le, Xiao Huang and Colin Zamecnik, who were there for me during both joyous and depressing moments during my graduate training. I am also grateful to the members of the Desai and Tang lab for their companionship, positive spirits, and collaborative atmosphere.

Lastly, I want to thank my parents for supporting me on this journey of scientific inquiry and medicine from the beginning. From a very early age, they have instilled diligent work ethics, resilience, curiosity and compassion into me. I am blessed with their hard work and love to receive the best education and the opportunity they have provided for me. Thank you to my siblings Calvin and Celine Chang for their companion and support throughout my graduate school years.

ABSTRACT

Therapeutic Nanotechnology and Immunoengineering for Cellular Therapy in Autoimmune Diabetes and Cancer

by

Ryan Chang

Cellular therapy has gained impressive momentum in recent years as has the promise to become the third pillar of biomedical therapeutics after small molecule and biologic drugs. Cells have capabilities that are significantly superior to traditional small molecule and biologics that are essential to tackling some of the most difficult to treat diseases. Only cells are able to sense their environments, engage in complex signal processing, and ultimately respond through motility, release of molecules, or engagement of other cell types to elicit a therapeutic response. Indeed, we have already witness exciting advances such as the use of chimeric antigen receptor engineered T cells to kill tumor cells, or the replacement of dysfunctional endogenous cells with stem cells to recapitulate a lost native biological function.

It is becoming increasingly clear that there is a role for biomaterials to play within the paradigm of cellular therapy to facilitate and augment its efficacy. The delivery of cellular products into patients is fundamentally different from the administration of small molecule or biologic drugs, and may

require the use of biomaterials for support to ensure optimal viability and function. In addition, material and device engineering may help overcome some challenges in protecting cellular therapeutic products from hazardous host environments, such as the immune response. Finally, materials may be engineered to interact with endogenous or exogenous cells to precisely instruct their fate and function. Here, we illustrate three projects that combine engineered biomaterials with cells as novel strategies to help us understand and overcome challenges in diabetes and in cancer therapy.

First, we demonstrate the fabrication and use of nanoengineered thin film polymer materials to encapsulate of stem cells for the treatment of diabetes. Through the engineer of nanopores in to encapsulation devices, we show the ability to exclude immune cells and prevent priming of the host immune system. Remarkably, encapsulated stem cell derived beta cells are viable up to 6 months and exhibit glucose sensitive insulin secretion *in vivo*.

Next, we illustrate the utility of a novel polymer scaffold to facilitate transplantation of islets into previously non-viable sites. In this study, we fabricated highly defined template patterns into polymer scaffolds to optimize islet cluster loading. We show the insulin secretion ability of islets loaded in scaffolds in well preserved. Finally, the islet-scaffold construct transplanted into the epidydimal fat pad successfully controlled blood glucose in diabetic mouse model.

In our final project, we synthesized nanoparticle tumor vaccines inspired by oncolytic viruses to treat solid tumors. Polymeric nanoparticles were loaded with a cocktail of immune adjuvants and a tumor antigen peptide. We demonstrate that these particles can efficiently present antigens to antigen presenting cells to instruct antigen specific T cell activation. Moreover, the polymeric nanoparticle vaccine successfully prevented the outgrowth of tumors in a syngeneic melanoma tumor model.

TABLE OF CONTENTS

List of Figures

I. Nanoporous immunoprotective Device for stem cell derived beta cell replacement therapy

A. ABSTRACT

Encapsulation of human embryonic stem cell differentiated beta cell clusters (hES-βC) holds great promise for cell replacement therapy for the treatment of diabetics without the need for chronic systemic immune suppression. Here, we demonstrate a nanoporous immunoprotective polymer thin film cell encapsulation device that can exclude immune molecules while allowing exchange of oxygen and nutrients necessary for in vitro and in vivo stem cell viability and function. Biocompatibility studies show the device promotes neovascular formation with limited foreign body response in vivo. The device also successfully prevented teratoma escape into the peritoneal cavity of mice. Long term animal studies demonstrate evidence of engraftment, viability and function of cells encapsulated in the device after 6 months. Finally, in vivo studies demonstrate that the device was able to effectively shield cells from the host immune system.

B. INTRODUCTION

Diabetes mellitus is a disease characterized by autoimmune mediated β-cell destruction in type 1 diabetes and progressive β-cell dysfunction in type

2 diabetes leading to insulin insufficiency. The current standard of care for diabetics relies on closely monitoring blood glucose levels and administration of exogenous insulin by injections to simulate natural insulin secretion kinetics of pancreatic β cells. However, exogenous insulin delivery often fails to adequately modulate blood glucose levels within a tight physiological range. Resulting complications include life-threatening hypoglycemic episodes and hyperglycemia induced long term micro and macro-angiopathies leading to cardiovascular pathologies, kidney failure, retinopathy, and neuropathy[1]. Pancreas and pancreatic islet transplantation has been proven to be an effective treatment modality for T1D patients to achieve insulin independence[2–4]; however, its use has been limited due to islet donor shortages and the need for chronic systemic immune suppression[5].

The development of human embryonic stem cell (hES) or induced pluripotent stem cells (iPSC)-derived insulin producing cells promises to address the challenge of islet donor shortage[6]. Although several groups have successfully produced insulin secreting cells from hES and iPSC [7–14], clinical translation requires new engineering solutions to address safety concerns of teratoma formation and protection against immune rejection[15]. Cell encapsulation has emerged as a promising strategy by providing a physical barrier between transplanted hES-derived beta cell clusters (hES-βC) and the transplant recipient, thereby achieving immunoprotection from the host

immune response[16,17]. The optimal cell encapsulation device should allow sufficient oxygen and nutrient exchange in order to support the viability of encapsulated cells. It should also allow for efficient transport of glucose and insulin so that blood glucose can be properly controlled. At the same time, immunoprotective cell encapsulation devices need to exclude penetration of immune cells, antibodies and pro-inflammatory cytokines. The devices must also be biocompatible and should confine any potentially tumorigenic cells.

Over the years, there have been several reports of macro or microencapsulation strategies for islet transplantation that have achieved varying degree of success[18–22]. A micro-encapsulation approach uses a polymer to individually contain a single cell or islet cluster within a microscale capsule, in order to maximize the surface area to volume ratio for improved nutrient exchange[23]. However, there is limited control over the thickness and pore size of microcapsules, and retrieval after injection is difficult. On the other hand, macro-encapsulation devices that contain many cells or islet clusters allow for much greater control over membrane thickness and pore size and can be readily retrieved after transplantation. However, these devices are suboptimal in nutrient exchange owing to thicker membranes and larger reservoir volume[24]. One of the most challenging issues is straddling the encapsulation device diffusional barrier between the limits of cell viability and adequate immune protection. It is useful to characterize the diffusional properties of cell

encapsulation barriers by their ability to transport immunoglobulins, pro-inflammatory cytokines, insulin, and glucose as a way of instructing future encapsulation device designs. In our previous work, we demonstrated the initial proof of concept of these thin film devices to encapsulate and protect immortalized MIN6 cell-line[25,26].

In this report, we incorporate hES-βC into an immunoprotective macro-encapsulation device. We specifically show that the membranes are able to exclude pro-inflammatory cytokines while allowing sufficient glucose and insulin exchange. Furthermore, we also demonstrate favorable long-term *in vivo* biocompatibility of the device as characterized by low foreign body response, robust neovasculature formation, and the ability to prevent cellular escape leading to teratomas. Encapsulated hES-derived insulin producing cells were shown to be viable and have measurable glucose sensitive c-peptide response in mice 6 months after transplantation. Finally, the immunoprotective devices successfully prevented the priming of antigen specific T cells *in vivo*.

C. METHODS

Nanoporous Immunoprotective Device Fabrication

Chemicals were purchased from Sigma-Aldrich unless noted. All films were spuncast onto silicon wafers at 1000 rpm for 30 s, followed by 2000 rpm for 30 s. Nanoporous polycaprolactone (80 kDa Mn) films were fabricated using an established template-based approach re- ported elseware[25]. In brief, a 0.5 M solution of zinc acetate dihydrate and ethanolamine in 2-methoxyethanol was spun- cast onto silicon wafers and annealed at 300 C on a hot plate to generate a zinc oxide (ZnO) seed layer. From this seed layer, ZnO nanorods were hydrothermally grown in a 5 mM zinc acetate solution at 85 to 90 C for 2 h. A 150 mg/mL PCL solution was then spuncast onto the nanorods, followed by a 150mg/mL PEG:PCL solution to provide a microporous support, creating a nanoporous film with a microporous backing support layer. The film was soaked in a dilute sulfuric acid solution to etch away the ZnO nanorods and also dissolve the PEG, resulting in a nanoporous membrane with pores ranging from 30 to 100nm supported by a microporous backing. Membrane characterizations and ZnO nanorod morphology were previously measured[25]. To assemble the device, two PCL thin-films heat-sealed together using resistive heating of a nichrome wire. A two-step heat-sealing method was used where 1.2 Amp current ran through a nichrome wire outlining the regions to be sealed. For the first sealing step, two films were placed over a U-shaped nichrome wire embedded in PDMS (Sylgard 184), 1 cm in diameter. To secure the membranes a PDMS weight was placed over the films holding them flat. A 1.2 Amp current ran through the wire for 15 seconds and sealed the devices in

the shape of a U, defining the device lumen shape and leaving an open side for cell injection. hSC-βC in high glucose Dulbecco's modified Eagle's (DME) were injected into the devices through the remaining open side and sealed by placing the open edge over a straight nichrome wire embedded in PDMS and heat-sealed with a 1.2 Amp current for 10 seconds.

Scanning Electron Microscopy

Nanoporous PCL thin films were mounted on a flat SEM mount with colloidal graphite (Ted Pella). Cross sections were flash-dipped in isopropanol, followed by liquid nitrogen freeze fracture and then mounted. Samples were imaged by Carl Zeiss Ultra 55 Field Emission Scanning Electron Microscope using an in-lens secondary electron detector at San Francisco State University.

Transwell Diffusion Assays

Standard Falcon brand 24 well 400 nm pore size PTFE transwell inserts barriers were kept intact (PTFE-400), or removed and replaced with 20 nm pore size or 200 nm pore size immunoprotective films (NIM-20, NIM-200). The inserts are then placed into respective wells on a 24 well plate. For transport studies, 0.3mL of 100μg/mL FITC conjugated dextran at 4kDa, 10kda, and 40KDa, 0.3mL of 100ug/mL human IgG, or 10mM glucose solution in PBS was placed in the top compartment. 1mL of PBS was placed in the bottom compartment. The transwell culture plate was placed in a 37C incubator and

left for 7 days or 5 minutes (glucose transport). Solution from the top and bottom compartments were sampled and concentration was quantified by fluorimeter. Glucose detection kit (ab102617) was used to determine the glucose concentrations. For cytokine diffusion studies, media from 48 hour cultured anti-CD3 and anti-CD28 activated splenocytes were collected and placed in the top compartment while fresh media was placed in the bottom compartment. After 7 day incubation at 37C, samples from both compartments were collected and quantified using mouse 31-plex cytokine Luminex kit.

Cell Culture

Isolation of mouse islets was performed as described[47]. Islets were cultured in RPMI 1640 supplemented with 10%(v/v) fetal bovine serum. Splenocytes were isolated from C57BL/6J mice by passing crushed spleen through a filter mesh and cultured in DMEM supplemented with 5% (v/v) fetal bovine serum. Undifferentiated Mel1$^{INS\text{-}GFP}$ cells[37] were maintained on mouse embryo fibroblast feeder layers (Milli- pore) in hESC media as described[13]. Suspension-based direct differentiations to generate hES-βC were carried out as described[8] with improvements to the last stage based on published reports[36,48].

Gene targeting of Mel1$^{INS\text{-}GFP}$ cells

To generate a cell line that expresses a constitutive firefly luciferase gene we employed recently published gene targeting approach of the insulated human

AAVS1 loci employing TALENs[45]. Briefly, we amplified a 6332 bp DNA piece containing all bacterial components, both homologies to the human AAVS1 loci, as well as the puromycin resistance gene from the Puro-Cas9 donor plasmid (Addgene #58409) and cloned a fragment consisting of a peptide cleavage site T2A, followed by the firefly luciferase gene and a poly A sequence in, to re-circulate the DNA piece. The resulting plasmid, termed Puro-T2A-Luc donor, was sequence verified by sanger sequencing. Confluent Mel1$^{INS\text{-}GFP}$ were dissociated to single cells and approximately 8,0x106 cells were mixed with 5ug of each of the TALEN plasmids and 20ug of the Puro-T2A-Luc donor in a 0,4cm gap electro-cuvette (Biorad). Cells were electroporated using a GenePulser (Biorad) using an exponential decay with 250V and 500uF settings. Targeted cells were plated on DR4 resistant MEFs and clones were selected with 0.5ug/ml Puromycin for 4 days. After 11-12 days, individual clones were manually picked and expanded before freeze down and genomic DNA analysis. gDNA was analyzed with primers for WT and correct Puro integration. WT/Puro Forward: CCG GAA CTC TGC CCT CTA AC, WT Reverse: AGA TGG CTC CAG GAA ATG GG, Puro Reverse: GTG GGC TTG TAC TCG GTC AT. Mel1$^{INS\text{-}GFP,AAVS1\text{-}Luc}$ line #3 was used for direct differentiation experiments.

Mice

NOD.Cg-Prkdcscid Il2rgtm1Wjl/SzJ mice (NSG) and C57BL/6J mice were obtained from Jackson Laboratories. Mice used in this study were maintained

according to protocols approved by the University of California, San Francisco Committee on Laboratory Animal Resource Center. For kidney capsule grafts, approximately 2.0×10^6 hESC-differentiated cells in clusters were transplanted as described[44]. For encapsulated grafts, approximately 2.0×10^6 hESC-differentiated cell clusters encapsulated in a bilaminar nanoporous immunoprotective device were transplanted in between the caudate and left hepatic lobe. For glucose-induced insulin secretion, mice were fasted overnight and serum was collected before and 1 hour after intraperitoneal administration of 3 g/kg D-glucose solution. Serum c-peptide levels were quantified by ELISA using commercially available kit (Alpco).

Flow Cytometric Analysis

Briefly, spheres were collected and allowed to settle by gravity. Clusters were washed once in PBS and dissociated by gentle pipetting after 12- to 15-min incubation in Accumax (innovative cell technologies). For flow-based analysis, dissociated cells were fixed with 4% paraformaldehyde (Electron Microscopy Science) for 15 min at room temperature, followed by two washes in PBS. Samples were either stored at 4C or immediately stained with directly conjugated antibodies. Data analysis was performed with FlowJo software. NKX6.1 – Alexa 647, PDX1-PE were obtained from BD Bioscience, and a human C-peptide antibody (Millipore, CHU-09) was in house conjugated to Alexa 488 fluorophore using a commercially available kit (Invitrogen)

Glucose-stimulated insulin secretion

Free and encapsulated hESC-derived spheres were transferred into tubes and washed twice with Krebs–Ringer Bicarbonate buffer (KRB) containing 2 mM glucose. Samples were incubated for 1 hour in 2 mM glucose containing KRB to allow equilibration of cells. 2 mM buffer was removed and replaced with fresh KRB containing 2 mM glucose for 30 minutes followed by incubation for another 30 minutes in KRB containing 20mM glucose. After the incubation period, buffers were collected for human C-peptide-specific ELISA analysis using a commercially available kit (Alpco).

Immunostaining

Mouse tissue samples were collected and fixed in 4% paraformaldehyde for 24 hours and washed with phosphate buffered saline at 4C for 48 hours, then 30% sucrose for 24 hours. Tissue samples were embedded in Optimal Cutting Temperature (OCT) and sectioned for staining. COL1A1, F4/80, and vWF antibodies were purchased from BD Biosciences.

In vivo Bioluminescence imaging

Nanoporous immunoprotective devices encapsulated with luciferase-expressing human embryonic cell derived pancreatic beta-like cell clusters (hSC-βC) were implanted in between the caudate and left hepatic lobes of the

liver of NOD.Cg- Prkdcscid Ill2rgtm1Wjl/SxJ (NSG) mice. Survival of the encapsulated cells in vivo was assessed by monitoring luciferase activity using a Xenogene IVIS 200 imaging system (PerkinElmer). The animals transplanted with hSC-βC cells were injected IP with D-luciferin solution (Goldbio, St. Louis,MO) at the dose of 150 mg/kg 5 min before imaging to capture the peak in bioluminescent intensity. The mice were anesthetized with an isoflurane mixture (2% in 98% O2) and imaged by using a Xenogen IVIS 200 imaging system. Bioluminescence images were acquired for 3 min and then analyzed using the Living Image analysis software (Xenogen, Alameda, CA). Regions of interest (ROI) were centered over the bioluminescence regions. Photons were counted within the ROI over the acquisition time. Adherence to the same imaging protocol ensured consistent signal detection on different days of in vivo imaging.

Cell Transfer

One day before cell transplantation, mice received Violet Proliferation Dye (VPD-450)-labeled lymph node (LN) cells from Ub-GFP-OT-1 Tg mice via retro-orbital injection as previously described[49]. 6 days after the transplant, pancreatic draining lymph node and the spleen were harvested and the proliferation of transferred T cells was determined using flow cytometry by measuring the dilution of CFSE. A Fortessa flow cytometer (BD Biosciences, San Jose, CA) and FACSDiva software (BD Biosciences) were used for flow

cytometric analysis. For sensitization of B57CL/6J mice, OVA expressing B16 melanoma cells were cultured overnight in DMEM media with serum washed twice in PBS. Cells were irradiated at 10 gy and 20×10^6 cells were injected IP or encapsulated into devices and transplanted into each recipient animal.

D. RESULTS

Immunoprotective Cell Encapsulation Device Design and Fabrication

The immunoprotective cell encapsulation device should allow for exchange of insulin, glucose, and oxygen while excluding immune cells, immunoglobulins, and proinflammatory cytokines across the membrane barrier (**Fig. 1a**). A bilaminar nanoporous thin film macroencapsulation device is a favorable design due to its ability to minimize inward transport of immune species through tightly controlled pore structures while the thin film barrier reduces the diffusional distance for optimal exchange of oxygen and nutrients. Proinflammatory cytokines interleukin-1beta(IL-1β), interferon-gamma (IFNγ), and tumor necrosis factor-alpha (TNFα) have hydrodynamic radii of 2.18 nm, 3.67 nm, and 3.80 nm respectively[27–29] ; Therefore, immunoprotective membranes require pore diameters on the order to 10 to 100 nm. Polycaprolactone, a synthetic polymer, was selected as the preferred material owing to its favorable physical and biocompatibility properties[30]. Unlike natural polymers such as sodium alginate that have batch-to-batch variations

and are often contaminated with endotoxins[31], synthetic polymer can be synthesized under reproducible and endotoxin free conditions[32]. Polycaprolactone has also been used in a variety of FDA approved medical products[30]. Furthermore, the low melting temperature of polycaprolactone allows for precise templating of stringently controlled pore sizes as well as tailored design of device geometry and thickness.

We fabricated nanoporous immunoprotective membranes (NIM) using a substrate templating technique (**Fig. 1b**)[25]. Briefly, zinc oxide nanorods were grown hydrothermally onto silicon wafers to yield structures measuring 20 nm in diameter and 500 nm in height (**Fig. 1c**). Polycaprolactone (PCL) solution was spin-cast onto zinc oxide nano-templated silicon substrates (**Fig. 1d**), followed by sulfuric acid etching of zinc oxide. The resulting polymer membrane is a 10 μm thick consisting of a 500 nm thick nanoporous layer backed by a supporting porous layer (**Fig. 1e**). To assemble the nanoporous immunoprotective device (NID) for cell encapsulation, 2 NIMs are cut to desired shapes and heat sealed at 70°C along the edges to form a bilaminar device with a patent lumen (**Fig. 1f**).

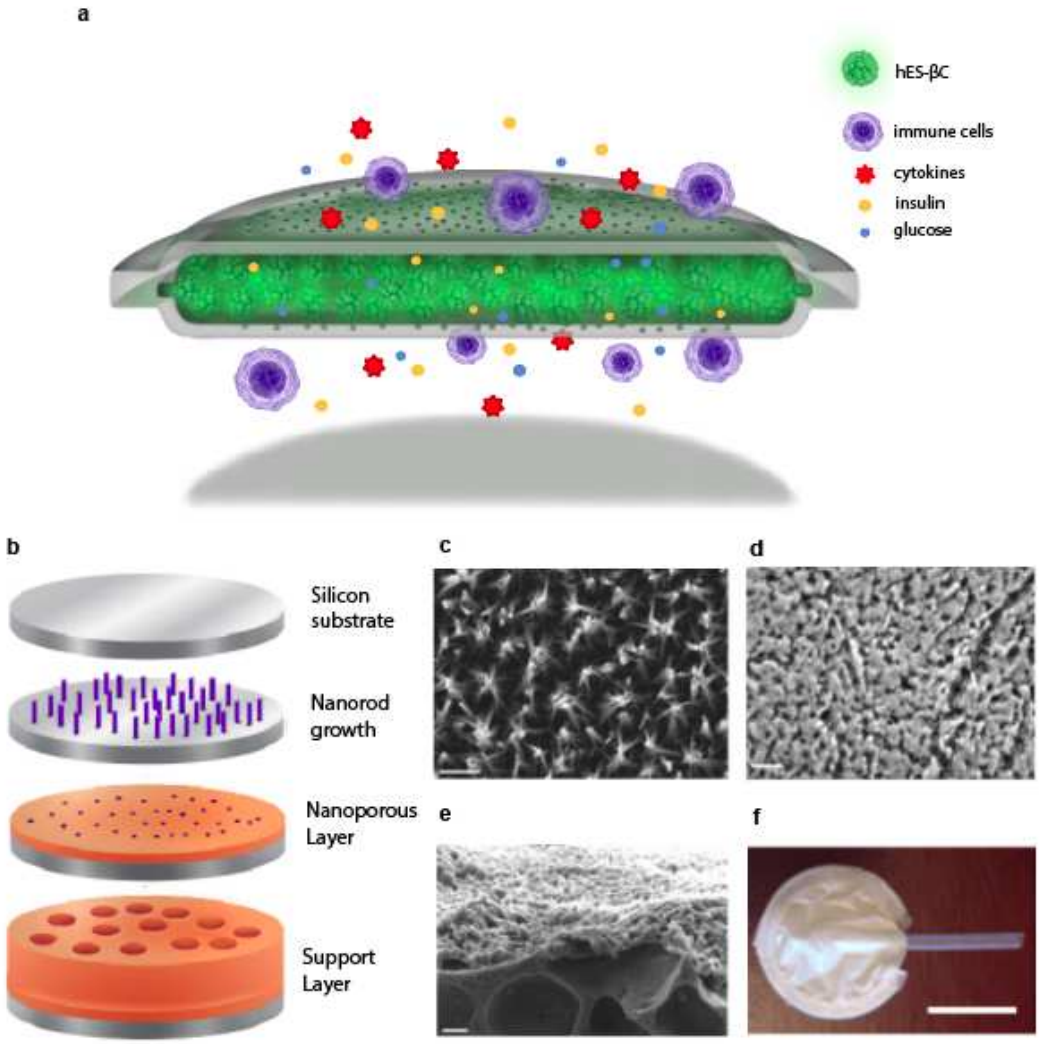

Figure 1.1 | Immunoprotective Cell Encapsulation Device Design and Fabrication. a, illustration of immune-protective cell encapsulation device. **b**, schematic illustration of fabrication process for nanoporous thin films by zinc oxide nanorod growths and polymer templating. c, scanning electron microscopy image of zinc oxide nanorod templated silicon substrate (scale bar = 100 nm). **d**, scanning electron microscopy image of cross-section of nanoporous caprolactone membrane (scale bar = 100nm). **e**, scanning electron

microscopy image of nanopores on surface of polycaprolactone membrane. **f,** assembled immunoprotective cell encapsulation device (scale bar = 1 cm).

In vitro characterization of nanoporous immunoprotective membranes

Immunoprotective barriers designed for cell encapsulation must selectively inhibit diffusion of key immunogenic molecules including immunoglobulins and pro-inflammatory cytokines while permitting exchange of glucose and insulin. Human IgG has a molecular weight of 153 kDa[33] while the TNF-alpha homotrimer, interferon-gamma, and interleukin 1- beta proinflammatory cytokines have molecular weights of 52kDa, 17kDa, and 30kDa respectively[27–29]. Twenty nm and 200 nm pore size NIMs (NIM-20 and NIM-200, respectively) were fabricated and characterized for their robust ability to prevent diffusion of immunoglobulins and proinflammatory cytokines. In addition, we included 400nm PTFE membranes (PTFE-400) with pore size comparable to the Theracyte device[34], the first macro-encapsulation device to be tested in clinical studies, as a control. We studied the molecular weight diffusion cut-off limit of NIMs and PTFE-400 by evaluating the diffusion rate of 4kDa, 10kDa, and 40kDa dextran molecules over a course of 7 days at physiological 37 C. Both NIM-20 and NIM-200, but not PTEF-400, were successful in preventing transport of 4kDa, 10kDa and 40kDa dextran molecules (**Fig 2a**). While NIMs are able to inhibit diffusion of high molecular weight cytokines, it is critical that they do not hinder the transport of smaller

molecules such as glucose. We measured the amount of glucose diffusion across NIM-20, NIM-200 and PTFE-400 over 5 minutes of 37C incubation. There was no significant difference between the amount of glucose transported across the 3 groups (**Fig. 2b**). These membrane characterization studies suggest that NIMs preferentially exclude larger molecular weight species such as immunoglobulin and proinflammatory cytokines while permitting the diffusion of smaller molecules, including glucose.

To determine if NIMs can selectively block immune molecules, we first investigated the ability of NIMs to inhibit diffusion of human IgG immunoglobulin over one week of 37C incubation. In this study, PTFE-400 failed to prevent transport of IgG while both NIM-20 and NIM-200 significantly reduced IgG transport (**Fig. 2c**). We furthered investigated which cytokines were preferentially excluded from diffusing into the cell containing compartment using a mouse pro-inflammatory cytokine Luminex panel[35]. We observed reduced cytokine diffusion across NIM-20 relative to NIM-200 or PTFE-400 barriers following a 7-day diffusion study (**Fig. 2d**). Interestingly, certain cytokines were excluded more effectively than others. For instance, only 10% of IL-1β was transported across NIM-20 while 25%, 80% of TNFα and IFNγ were transported across the same NIM-20 respectively. One may expect a size dependent relationship that can explain the diffusion profile of our panel of pro-inflammatory cytokines. Cytokine diffusion rates were

compared against their respective protein molecular weights (**Fig. 2e**). Although there was a general trend toward reduced diffusion with larger molecular weight cytokines, there exist a population of small molecular weight cytokines with poor transport kinetics. One of the properties explaining this phenomenon could be differences in protein charges as the negatively charged polycaprolactone NIMs[30] can preferentially cause adhesion of positively charged cytokines. Indeed, isoelectric point of cytokines had a significant effect on the protein's ability to transport across NIMs. Specifically, cytokines with isoelectric points above 7 that are positively charged at neutral pH transported poorly across NIMs regardless of their molecular weight while negatively charged cytokines exhibited size dependent transport kinetics (**Fig. 2e**). Electrostatic repulsion between the cytokines and the surface of the polymer nanopores potentially allow negatively charged cytokines to traverse through the nanoporous structures of NIMs more effectively.

Since cytokine diffusion is attenuated, we then further determined if NIMs offer pancreatic islets protection against cytokine exposure. In a transwell coculture system, mouse islets were placed in the top compartment while syngeneic mouse splenocytes activated by surface immobilized anti-CD3 and anti-CD28 were placed in the bottom compartment as a source of cytokines. The top and bottom compartments were separated by NIM-20, NIM-200 or a 8 μm PTFE barrier (PTFE-8000). The viability of mouse islets was

quantified 48 hours later using flow cytometry of dissociated islets after propidum iodine staining. Results of this study demonstrate significantly reduced apoptosis in mouse islets protected by NIM-20, and NIM-200 when compared to islets protected by PTFE-8000 (**Fig. 2f**). Consistent with our results shown in **Fig. 2d**, we confirmed that NIM-20 reduced proinflammatory cytokine diffusion into the islet compartment (**Supplementary Fig. 1a)**.

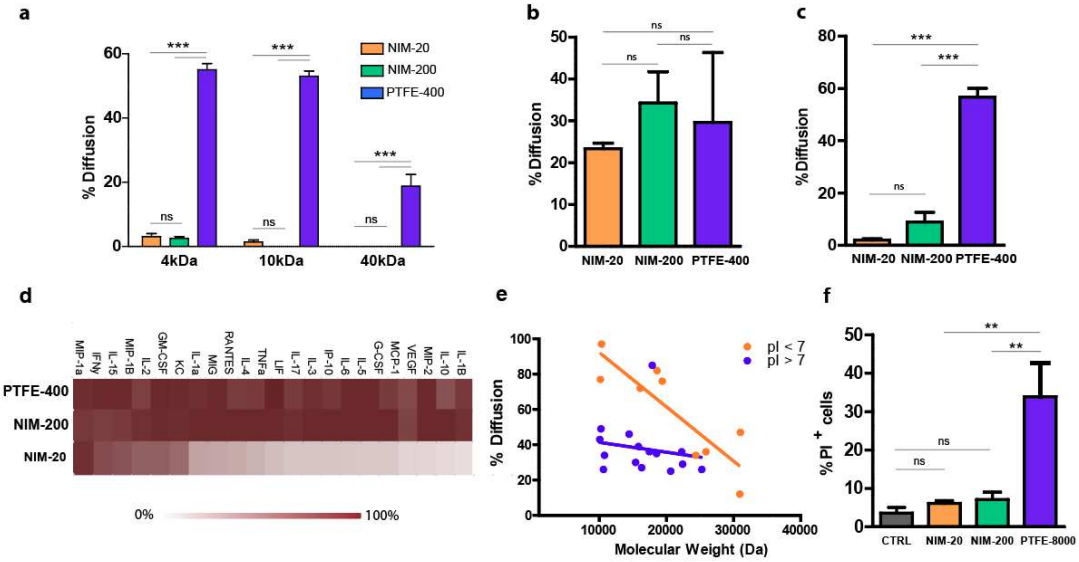

Figure 1.2 | *In vitro* characterization of nanoporous immunoprotective membranes. a, 4kDa, 10kDa, 40kDa FITC-dextran diffusion rate across NIM-20, NIM-200, and PTFE-400 pore size films over 7d (n=5 per group). **b**, 5-minute glucose diffusion rate across NIM-20, NIM-200, and PTFE-400. (n=5 per group) **c**, FITC-IgG diffusion rate across, NIM-20, NIM-200, PTFE-400 films over 7d. (n=6 per group) **d**, Quantification of transwell pro-inflammatory cytokine diffusion across NIM-20, NIM-200, and PTFE-400 over 7d measured

by Luminex. **e**, Cytokine diffusion rate for NIM-20 compared to molecular weight and protein charge. **f**, Propidium iodine staining of dissociated islets recovered from coculture with anti-CD3/CD28 activated splenocytes isolated from wildtype C57BL6/J mice separated by NIM-20, NIM-200, PTFE-8000 or no splenocyte control (ctrl) over a 48 hrs period. (n=3 per group). *P < 0.05, **P < 0.01, ***P < 0.001.

In vitro evaluation of cell viability and function in nanoporous immunoprotective device

Once establishing that the exclusion of cytokines and immunoglobulins is important for preservation of primary mouse islet viability, we evaluated the ability of NIDs to support the viability and function of encapsulated human stem cell derived beta cell clusters (hES-βC) as a more relevant system for cell therapy approaches. hES-βC cells were generated by a direct differentiation approach previously described[8] with modifications of the last stage based on published work[14,36]. To facilitate the detection of hES-βC, we generated them from Mel1 human embryonic stem cells that contain a GFP reporter driven under the endogenous insulin promoter[37]. Using this cell line, endogenous insulin expression, and thus beta cell viability, can be followed live by measuring the GFP fluorescence signal. Differentiated clusters consist of approximately 35% hES-βC cells as identified by intracellular flow analysis for human C-peptide as a readout of endogenous insulin production (**Fig. 3a)**. In

addition, virtually all hES-βC cells co-express key β-cell transcription factors PDX1 and NKX6.1 (**Fig. 3a**), shown to be critical for beta cell function and maintenance[38,39]. To further characterize our NIMs, we delivered hES-βC 300 clusters to the luminal cavity of a partially sealed NID and are then fully encapsulated by localized heat sealing (**Fig. 3b**). Importantly, fluorescence intensity from NID encapsulated hES-βC was stable in both NID-20 and NID-200 over a course of 5 weeks *in vitro* (**Fig. 3c, Supplementary Fig. 2a**). This result demonstrates that insulin expression and thus viability of hES-βC encapsulated in NID can be maintained in culture over prolonged periods of time. We further studied the ability of NID encapsulated hES-βC to secrete insulin in response to glucose stimulations. Interestingly, both NID-20 and NID-200 encapsulated hES-βC exhibited glucose stimulated insulin secretion with comparable glucose stimulation indices (GSI) of approximately 1.5 (**Fig. 3d, e**). While these data are within the range of GSI reported previously[8,14,36], it is likely that insulin diffusion was somewhat restricted as we observed reduced C-peptide concentration in both high and low glucose buffers in the smaller pore size NID-20 compared to that of NID-200. Based on these results, we continued our studies with NID-200 since it represents a more ideal encapsulation device for further animal studies as it protected islets against immunological challenges and allowed better diffusion of small molecules, including insulin and glucose.

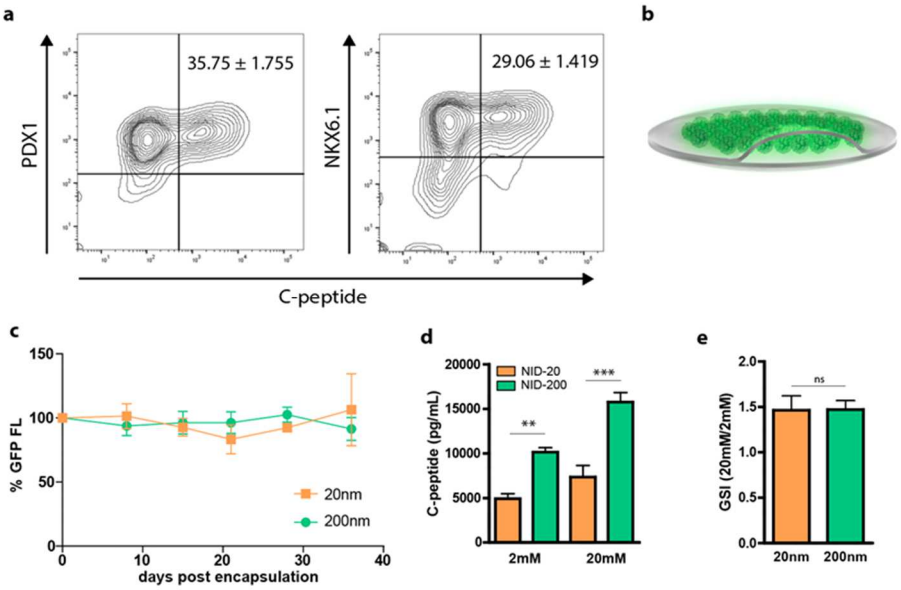

Figure 1.3 | *In vitro* evaluation of cell viability and function in nanoporous immunoprotective device. a, cytoflow based co-analysis of intracellular beta cell transcription factors PDX1, NKX6.1 and the endogenous insulin synthesis marker C-peptide. (n=8) **b,** Illustration of encapsulated hES$^{INS\text{-}GFP}$ derived beta-cell containing clusters in bilaminar thin film device. **c**, GFP fluorescence signal (FL) measured from hES$^{INS\text{-}GFP}$-βC that were encapsulated in NID-20 and NID-200 and cultured for > 5 weeks *in vitro*. (n=4) per group. **d**, glucose stimulated insulin secretion assay for NID-20 and NID-200 encapsulated hES$^{INS\text{-}GFP}$-βC analyzed by human C-peptide specific ELISA .(n=4 per group) **e**, glucose stimulation index (GSI, 20mM/2mM glucose for 30 minutes) of NID-20 and NID-200 encapsulated hES$^{INS\text{-}GFP}$-βC. (n=4 per group). *P < 0.05, **P < 0.01, ***P < 0.001.

***In vivo* NID biocompatibility and prevention of teratoma escape.**

Biocompatibility of biomaterials has been shown to be critical for the safety and integrity of long term cell encapsulation devices[40]. In particular, foreign body responses and fibrous capsule development following implantation of medical devices need to be carefully studied for NIDs. Protein adsorption on material surfaces can promote macrophage recruitment to the tissue-material implant site which may become activated through the alternative pathway and enhance fibrogenesis by fibroblasts, leading to fibrous capsule formation around the implant[41,42]. To study this property, we incubated PCL and PTFE surfaces in fetal bovine serum for 24h and demonstrate similar levels of protein adsorption on both material surfaces (**Supplementary Fig. 3a**). An ideal biomaterial for cell encapsulation implant devices should exhibit low macrophage recruitment and fibrosis at the material-tissue interface while also permitting the formation of neovasculature along the surface of the material to provide oxygen and nutrient support for the encapsulated cells. To this end, polycaprolactone (PCL) and polypropylene (PP) films were implanted subcutaneously into immunocompetent C57BL/6J mice as part of a long term in vivo biocompatibility study. PCL films along with surrounding tissue were explanted at 4 months followed by tissue sectioning and staining for Collagen 1, a macrophage marker (F4/80), and von Willibrand Factor to elucidate fibrosis, macrophage recruitment and angiogenesis, respectively. Immunostainings show increased blood vessel formation and reduced fibrosis and macrophage recruitment in PCL film grafts compared to

PP implants (**Fig. 4a**). This data is in agreement with H&E staining (**Supplementary Fig. 4a, b**) that showed minimal fibrosis following 4 month subcutaneous transplant in immunocompetent mice, and suggests that PCL thin films exhibit favorable biocompatibility leading to robust neovasculature formation in the absence of chronic foreign body response.

The use of cell encapsulation devices for the transplantation of human stem cell products is important due to regulatory safety considerations in the event of cell escape, dedifferentiation, and/or teratoma formation. Macro-encapsulation devices are advantageous over microencapsulation strategies because they prevent the distribution of stem cells throughout the body and allow for easier retrieval of explant. This is particularly important for the prevention of teratomas which can arise from hES cells that are not fully differentiated[43]. We modeled the formation of teratomas *in vivo* by transplanting either encapsulated or naked undifferentiated hES into immune deficient NOD scid gamma (NSG) mice. Encapsulated hES cells were transplanted between the caudate lobe and left hepatic lobe while naked cells were delivered under the kidney capsule in order to confine their location within the animal[44]. To be able to efficiently monitor hES cells after transplantation into animals, we engineered a constitutively expressed firefly luciferase gene into the insulated human AAVS1 loci of Mel1$^{INS\text{-}GFP}$ using TALENS as previously described[45] (**Supplementary Fig. 5**, henceforth

referred to as Mel1$^{INS\text{-}GFP;AAVS1\text{-}Luc}$). Six weeks following transplantation, we observed pervasive teratomas in the animals that were transplanted with naked hES under the kidney capsule and an increase in body weight indicative of increased tumor mass in these animals (**Fig. 4b, c)**. In addition, imaging of luciferase signal demonstrates the confinement of encapsulated cells, while naked Mel1$^{INS\text{-}GFP;AAVS1\text{-}Luc}$ escaped the kidney capsule and were detected throughout the peritoneal body cavity **(Fig. 4d,e**). Taken together, these data demonstrate the ability of our PCL NID encapsulation approach to contain proliferative cell populations within the device and prevent them from spreading throughout the body.

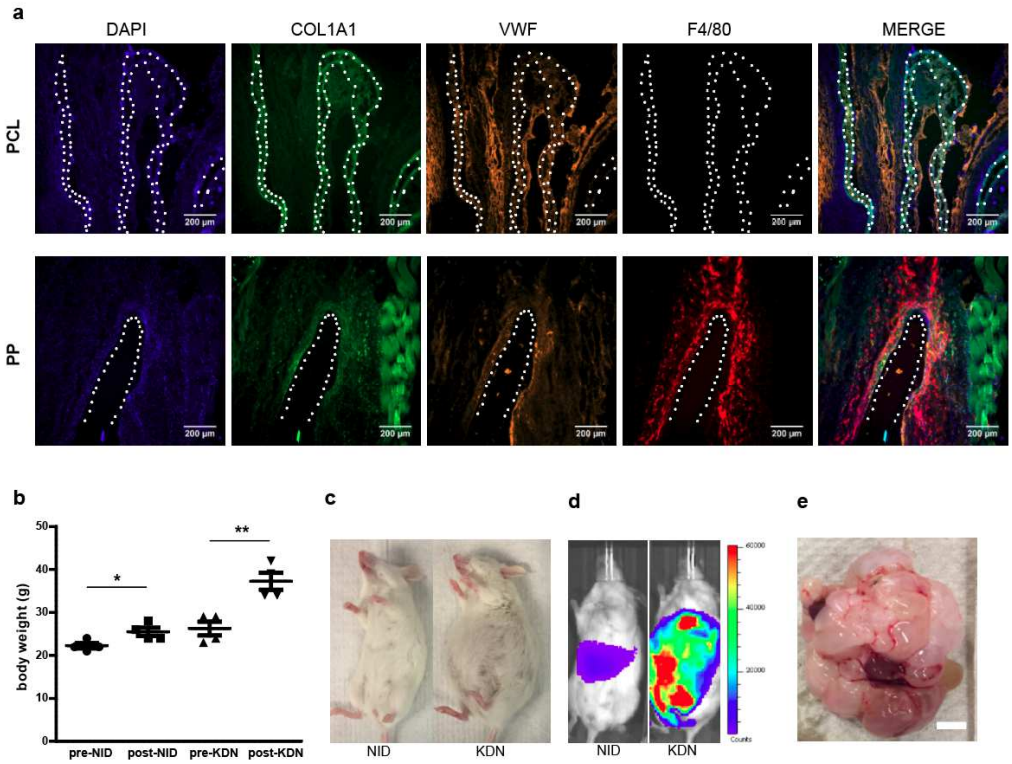

Figure 1.4 | *In vivo* NID biocompatibility and prevention of teratoma escape. a, immunofluorescent staining for collagen (COL1A1), neo-vasculature (VWF), and macrophage (F4/80) markers of 4 month subcutaneous polycaprolactone and polypropylene thin films implants in C57BL/6J mice. **b,** day 0 and week 6 body weight measurements from mice transplanted with undifferentiated Mel1$^{INS\text{-}GFP;AAVS1\text{-}LUC}$ cells in NID or naked under the kidney capsule of NSG mice. (n=4 per group). *P < 0.05, **P < 0.01, ***P < 0.001. **c**, gross image of mice that received undifferentiated Mel1$^{INS\text{-}GFP;AAVS1\text{-}LUC}$ cells transplants either encapsulated devices (NID) or naked (KDN) under the kidney capsule of NSG mice. **d**, representative bioluminescence image of NSG mice transplanted with undifferentiated Mel1$^{INS\text{-}GFP;CON\text{-}LUC}$ cells either encapsulated (NID) or naked (KDN) under the kidney capsule of NSG mice after 6 weeks. **e**, representative gross morphology image of explanted teratoma mass from undifferentiated, naked Mel1$^{INS\text{-}GFP;AAVS1\text{-}LUC}$ cells (scale bar = 1cm).

In vivo viability and function of hES-βC encapsulated in NID

To study viability and function of encapsulated Mel1$^{INS\text{-}GFP;AAVS1\text{-}Luc}$ derived hES-βC into NID, we transplanted them between the caudate lobe and left hepatic lobe of NSG mice, as this site was determined to be the most optimal transplant site for cell survival (**Supplementary Fig. 6a,b**). We then measured graft persistence using bioluminescence imaging of the

constitutively expressed luciferase gene. Luciferase bioluminescence in mice transplanted with NID encapsulated hES-βC was detected on day of transplantation as well as 30 days, and 6 months after transplantation (**Fig. 5a, e**). These results are in agreement with our *in vitro* data showing that NIDs allow the long-term survival of hES-βC cells. To assess the functional properties of encapsulated hES-βC one week post transplantation, mice were fasted overnight, followed by a challenge consisting of a bolus of glucose via intraperitoneal injection. Glucose stimulated c-peptide production can be seen one week after transplantation into NSG mice and remained constant at the 6 months (**Fig. 5b**). The long-term function of NID encapsulated grafts was similarly assessed. Mouse serum was collected following overnight fast and one hour after intraperitoneal glucose challenge and measured for human c-peptide concentration. Glucose stimulated c-peptide secretion can be demonstrated in all mice and glucose stimulation index ranged from 2 to 7 (**Fig. 5c, d**). Explantation of NID devices containing hES-βC cells after 6 months followed by immunostaining for human C-peptide shows islet-like clusters within the device (**Fig. 5f**). Collectively, these studies show that NIDs are capable of supporting the viability and function of hES-βC in vivo for at least 6 months.

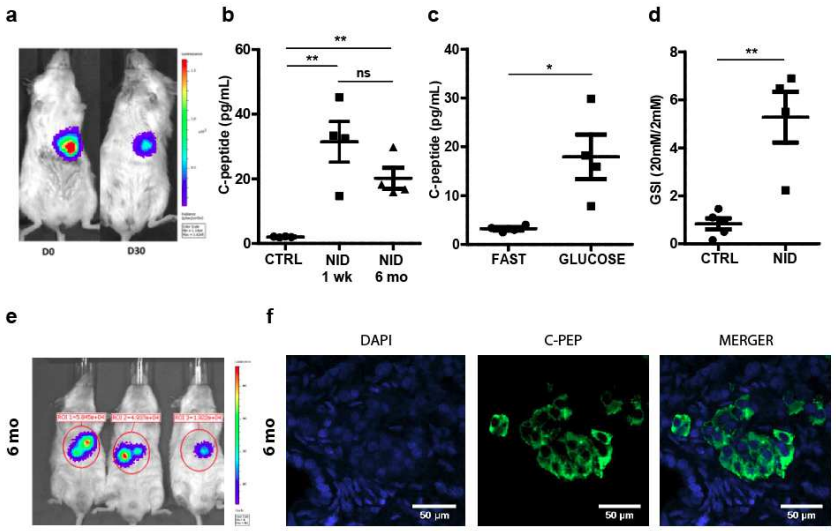

Figure 1.5 | *In vivo* viability of function of hES-βC encapsulated in NID. **a**, representative bioluminescence image of NSG mice transplanted with NID encapsulated hES$^{INS\text{-}GFP;AAVS1\text{-}LUC}$ –βC between liver lobes at d0 and d30. **b**, human C-peptide concentration in mouse sera after 60 minutes IP glucose challenge of over-night fasted mice one week and six months post-transplantation of NID encapsulated (NID) or untransplanted mice (CTRL). (n=4 per group) **c**, human C-peptide concentration in mouse sera after 60 minutes IP glucose challenge of over-night fasted mice 6 months post-transplantation of NID encapsulated or naked hES$^{INS\text{-}GFP;AAVS1\text{-}LUC}$-βCs. (n=4 per group) **d**, glucose stimulation index (GSI) of NID encapsulated or naked hES$^{INS\text{-}GFP;AAVS1\text{-}LUC}$-βCs (CTRL) 6 months post-transplantation. (n=4 per group). *P < 0.05, **P < 0.01, ***P < 0.001. **e**, representative bioluminescence image of NSG mice transplanted with NID encapsulated hES$^{INS\text{-}GFP;AAVS1\text{-}LUC}$-βCs after 6 months. **f**, representative immunofluorescence staining of NID encapsulated

hES$^{INS\text{-}GFP;AAVS1\text{-}LUC}$-βCs for human C-peptide (C-PEP) 6 months post transplantation. Nuclei are visualized by DAPI staining.

In vivo evaluation of immunoisolation by NID encapsulation

Since T cells are the principal drivers of alloimmune rejection of grafts, immunoprotective cell encapsulation devices must be able to prevent their activation. To maximally assess the immunoisolation capability of NIDs *in vivo*, we measured activation of antigen specific T cells in response to mice challenged with ovalbumin (OVA) expressing B16 cells encapsulated in NIDs. OVA-specific CD8+ T cells were collected from lymph nodes of OT-1 T cell receptor transgenic mice[46], stained with VPD-450, and adoptively transferred into wild-type C57BL/6J mice. The mice then received an intraperitoneal challenge of 2×10^7 free or NID encapsulated OVA-expressing B16 melanoma cells. Six days following challenge, draining lymph nodes and spleen were harvested and analyzed for the proliferation of OT1 OVA specific T cells (**Fig. 6a**). Flow cytometric analysis revealed loss of VPD-450 dye in mice with an unprotected B16-OVA challenge transplant, indicating extensive proliferation of OT1 cells; however, proliferation of OT1 T cells was minimal in mice that have been challenged with encapsulated B16-OVA cells (**Fig. 6b**). Animals transplanted with encapsulated B16-OVA cells had significantly reduced OVA-specific T cell proliferation in both the spleen and draining lymph nodes (**Fig. 6c, d**). Moreover, there was no significant difference between the median

fluorescent intensity of OVA-specific T cell populations in animals that received NID encapsulated B16-OVA cells when compared to animals that did not receive any B16-OVA cells (**Fig. 6e, f**). These results definitively demonstrate absence of allogeneic antigen specific T cell priming in hosts that received encapsulated cell transplants.

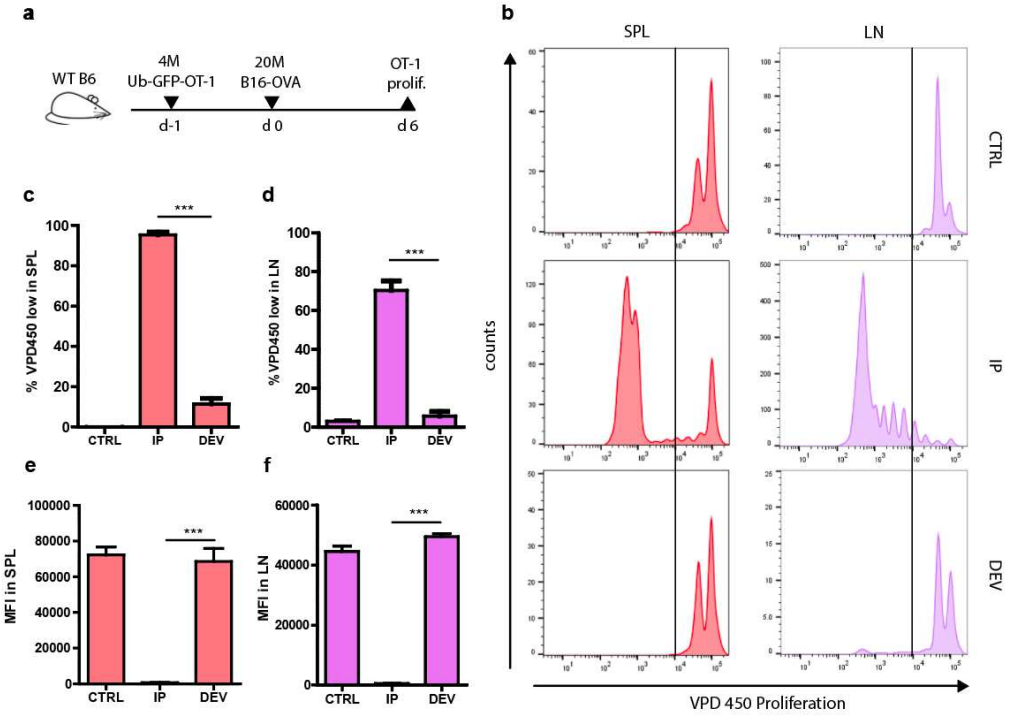

Figure 1.6 | *In vivo* evaluation of immune-isolation by NID encapsulation. **a-f,** Wild-type C57BL/6J mice were adoptively transferred with 4×10^6 OT1 expressing $CD8^+$ T cells. The following day mice received transplants of either NID encapsulated or naked B16-OVA cells in the peritoneum. Spleen and draining lymph node were harvested 6 days later for analysis. a, schematic outlining the experimental approach. **b,** representative cell proliferation dye

dilution graphs of $GFP^+/CD8^+$ T cells isolated from the spleen and lymph nodes of control mice (CTRL) or naked (IP) or NID encapsulated (DEV) B16-OVA cells. (n=3 per group) **c,** quantification of proliferating antigen-specific T cells isolated from spleens of mice from CTRL, IP, and DEV conditions. (n=3 per group) **d,** quantification of proliferating antigen-specific T cells isolated from draining lymph nodes of mice from CTRL, IP, and DEV conditions. (n=3 per group) **e,** median fluorescence intensity measurement of $GFP^+/CD8^+$ T cells isolated from spleens of mice from CTRL, IP, and DEV conditions. (n=3) **f,** median fluorescence intensity measurement of $GFP^+/CD8^+$ T cells isolated from draining lymph nodes of mice from CTRL, IP, and DEV conditions. (n=3 per group). $^*P < 0.05$, $^{**}P < 0.01$, $^{***}P < 0.001$.

E. DISCUSSION

Stem cell replacement therapy has the potential to fundamentally change the way we treat and manage diabetes by achieving insulin independence in patients. Significant progress has been made in developing human stem cell derived insulin producing cells[7–14], but ultimately stem cell products benefit from integration with device strategies in order to overcome translational challenges in cell delivery, engraftment, immunoprotection, and safety[17]. Although there have been several encouraging reports of encapsulation strategies achieving glucose correction in animal models, we

still have much to learn about the engineering specifications necessary for successful cell engraftment and immunoprotection.

In this report, we systematically evaluate a bilaminar synthetic polymer nanoporous immunoprotective cell encapsulation device (NID) for its ability to immunoprotect, and sustain the function and viability of human stem cell derived beta cells both *in vitro* and *in vivo*. The use of stem cell derived beta cell products in this study mitigates existing islet donor shortages, and potentially enables more diabetic patients to receive cell replacement therapy. Macro-encapsulation devices offer distinct translational advantages of teratoma confinement and retrievability compared to micro-encapsulation alternatives. Microencapsulation approaches using sodium alginate typically experience thick fibrous capsule formation, while macro-encapsulation NIDs in our study show robust neovascularization with minimal foreign body response after long term implantation. Immunoisolation studies demonstrate NIDs can robustly prevent antigen specific T cell priming. Most importantly, six-month animal studies demonstrate that hSC-βC in NID are both glucose responsive and viable with a GSI index that exceeds the minimum standard for islet transplantation currently performed clinically. A better understanding of the parameters necessary for efficient engraftment and immunoprotection of cells in encapsulation devices will greatly improve the chances of successfully bringing beta-cell replacement therapies into the clinic.

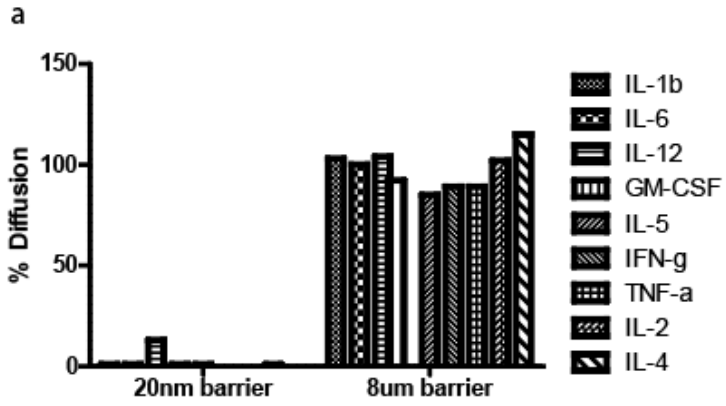

Fig. S1.1, **Cytokine diffusion across immunoprotective barrier after splenocyte-islet transwell culture. a,** Luminex quantification of mouse-proinflammatory cytokine diffusion rate across 20 nm pore size PCL films and 8 μm pore size PTFE films from the basolateral activated splenocyte containing compartment into the apical islet compartment.

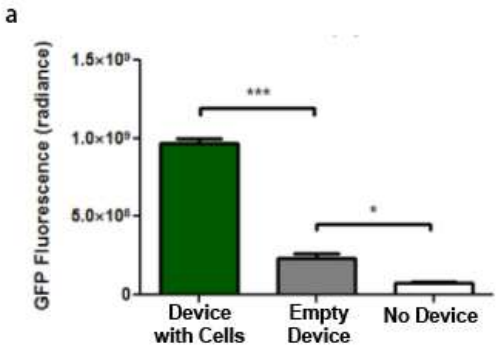

Fig. S1.2, Evaluation of GFP fluorescence intensity of encapsulated human stem cell derived beta cell clusters (hES-βC) containing GFP reporter driven under the endogenous insulin promoter. **a,** GFP fluorescence was measured by in vivo imaging system (Caliper) from device encapsulated with hES-βC, devices without any cells, and no device background control. (n=4)

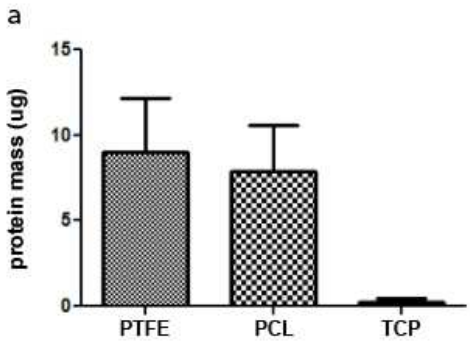

Fig. S1.3, **Characterization of protein adsorption on material surfaces**. **a,** Quantification of protein mass adsorbed onto 1.5 cm diameter PTFE, PCL, or tissue culture plastic (TCP) material surfaces following 24 hours of incubation in fetal bovine serum. (n=14)

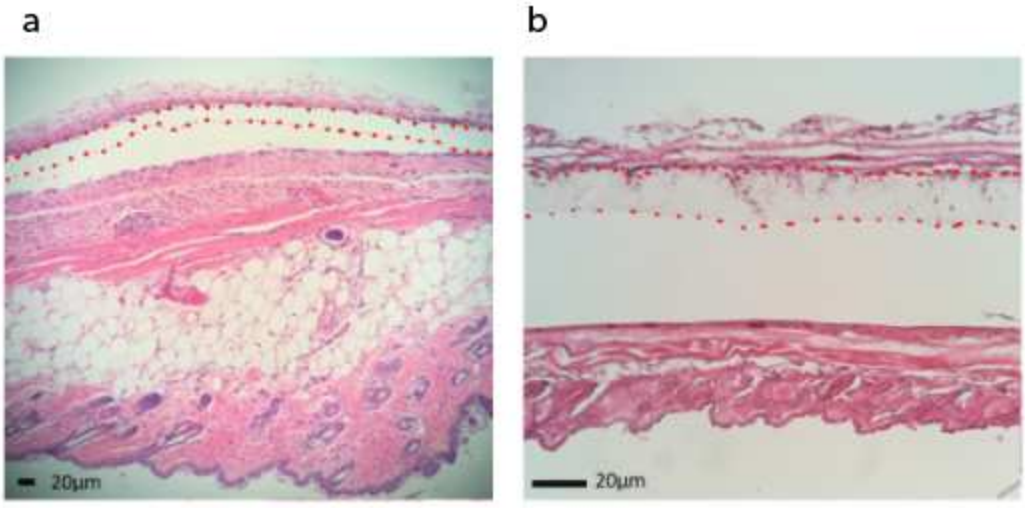

Fig. S1.4, Assessment of biocompatibility following subcutaneous implantation. **a,** H&E staining of polypropelene films implanted subcutaneously into immunocompetent C57BL/6J mice for 2 weeks. **b,** H&E

staining of polycaprolactone thin films implanted subcutaneously into immunocompetent C57BL/6J mice for 4 months.

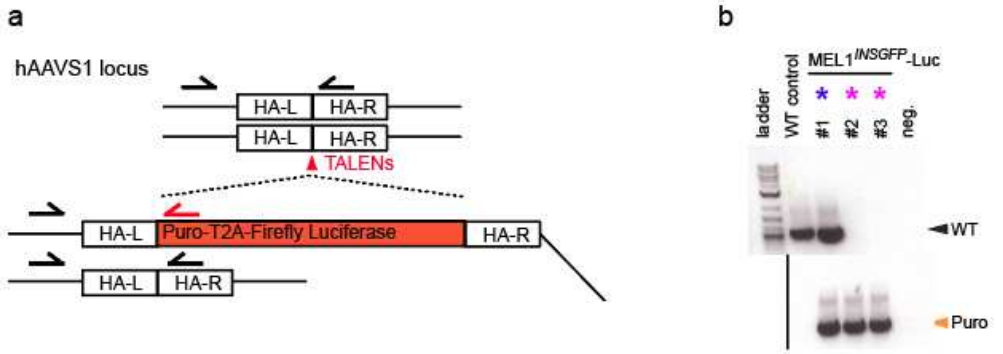

Fig. S1.5, Generation of hES$^{INS\text{-}GFP;AAVS1\text{-}LUC}$ cell line. a. Schematic illustrating the targeting strategy employed. b. gDNA PCR analysis with primers specific for the wild type (WT, black arrows) AAVS1 DNA sequence and site specific integrated Puro-T2A-Luc donor plasmid (Puro, black and red arrows). WT control is gDNA from hES$^{INS\text{-}GFP}$ cells, no template control is neg. Blue and pink stars indicate heterogeneous (#1) and homologous clones (#2, and #3), respectively.

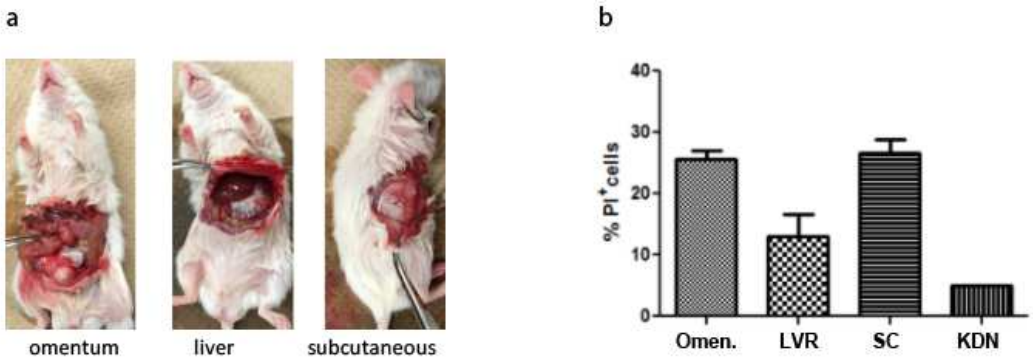

Fig. S1.6, Assessment of optimal transplant site for NID encapsulated hES-βC. **a,** representative image of NID transplanted in the omentum(Omen.), liver(LVR), subcutaneous space (SC). **b,** propidium iodine staining of retrieved cells from NID following 1 week transplantation. (n=3)

F. REFERENCES

(1) Melendez-ramirez, L. Y.; Cefalu, W. T.; Richards, R. J. Complications of Type 1 Diabetes. *Endocrinol. Metab. Clin. NA* **2010**, *39*, 625–640.

(2) Shapiro, A. M.; Lakey, J. R.; Ryan, E. A.; Korbutt, G. S.; Toth, E.; Warnock, G. L.; Kneteman, N. M.; Rajotte, R. V. Islets Transplantation in Seven Patietns with Type 1 Diabetes Mellitus Using a Glucocorticoid-Free Immunosuppressive Regimen. *N. Engl. J. Med.* **2000**, *343*, 230–238.

(3) Frassetto, A.; Masharani, U.; Kerlan, R. K.; Fong, L.; Vincenti, F. G.; Surgery, T.; Francisco, S.; Francisco, S.; States, U. Islet Transplantation in Type 1 Diabetics Using an Immunosuppressive Protocol Based on the Anti-LFA-1 Antibody Efalizumab. *Am J Transplant.* **2010**, *10*, 1870–1880.

(4) Symposium, D. C. Improvement in Outcomes of Clinical Islet Transplantation: 1999 – 2010. **2012**, *35*.

(5) Ryan, E. A.; Paty, B. W.; Senior, P. A.; Bigam, D.; Alfadhli, E.; Kneteman, N. M.; Lakey, J. R. T.; Shapiro, A. M. J. Five-Year Follow-Up After Clinical Islet Transplantation. **2005**, *54*.

(6) Bouwens, L.; Houbracken, I.; Mfopou, J. K. The Use of Stem Cells for Pancreatic Regeneration in Diabetes Mellitus. *Nat. Publ. Gr.* **2013**, *9*, 598–606.

(7) Zhou, Q.; Brown, J.; Kanarek, A.; Rajagopal, J.; Melton, D. A. In Vivo Reprogramming of Adult Pancreatic Exocrine Cells to B -Cells. **2008**, *455*.

(8) Russ, H. A.; Parent, A. V; Ringler, J. J.; Hennings, T. G.; Nair, G. G.; Shveygert, M.; Guo, T.; Puri, S.; Haataja, L.; Cirulli, V.; *et al.* Controlled Induction of Human Pancreatic Progenitors Produces Functional Beta-like Cells in Vitro. **2015**, *34*, 1759–1772.

(9) Hebrok, M. Generating β Cells from Stem Cells-the Story so Far. *Cold Spring Harb. Perspect. Med.* **2012**, *2*, a007674.

(10) Nostro, M. C.; Keller, G. Seminars in Cell & Developmental Biology Generation of Beta Cells from Human Pluripotent Stem Cells : Potential for Regenerative Medicine. *Semin. Cell Dev. Biol.* **2012**, *23*, 701–710.

(11) D'Amour, K. a; Agulnick, A. D.; Eliazer, S.; Kelly, O. G.; Kroon, E.; Baetge, E. E. Efficient Differentiation of Human Embryonic Stem Cells to Definitive Endoderm. *Nat. Biotechnol.* **2005**, *23*, 1534–1541.

(12) Van Hoof, D.; Mendelsohn, A. D.; Seerke, R.; Desai, T. a; German, M. S. Differentiation of Human Embryonic Stem Cells into Pancreatic Endoderm in Patterned Size-Controlled Clusters. *Stem Cell Res.* **2011**, *6*, 276–285.

(13) Guo, T.; Landsman, L.; Li, N.; Hebrok, M. Factors Expressed by Murine Embryonic Pancreatic Mesenchyme Enhance Generation of Insulin-Producing Cells from hESCs. *Diabetes* **2013**, *62*, 1581–1592.

(14) Rezania, A.; Bruin, J. E.; Arora, P.; Rubin, A.; Batushansky, I.; Asadi, A.; O'Dwyer, S.; Quiskamp, N.; Mojibian, M.; Albrecht, T.; *et al.* Reversal of Diabetes with Insulin-Producing Cells Derived in Vitro from Human

Pluripotent Stem Cells. *Nat. Biotechnol.* **2014**, *32*, 1121–1134.

(15) Steele, J. a M.; Hallé, J.-P.; Poncelet, D.; Neufeld, R. J. Therapeutic Cell Encapsulation Techniques and Applications in Diabetes. *Adv. Drug Deliv. Rev.* **2013**.

(16) Soon, P.; Feldmant, E.; Nelson, R.; Heintz, R.; Yao, Q.; Yao, Z.; Zheng, T.; Merideth, N.; Skjak-braek, G.; Espevik, T.; *et al.* Long-Term Reversal of Diabetes by the Injection of Immunoprotected Islets. **1993**, *90*, 5843–5847.

(17) Desai, T.; Shea, L. D. Advances in Islet Encapsulation Technologies. *Nat. Publ. Gr.* **2016**.

(18) Pepper, A. R.; Pawlick, R.; Gala-lopez, B.; Macgillivary, A.; Mazzuca, D. M.; White, D. J. G.; Toleikis, P. M.; Shapiro, A. M. J.; Frc, F. E. Diabetes Is Reversed in a Murine Model by Marginal Mass Syngeneic Islet Transplantation Using a Subcutaneous Cell Pouch Device. **2015**, *99*.

(19) Microencapsulated Islets as Bioartificial Endocrine Pancreas Author (S): Franklin Lim and Anthony M . Sun Published by : American Association for the Advancement of Science Stable URL : http://www.jstor.org/stable/1684447. **2016**, *210*, 908–910.

(20) Duvivier-Kali, V. F.; Omer, a; Parent, R. J.; O'Neil, J. J.; Weir, G. C. Complete Protection of Islets against Allorejection and Autoimmunity by a Simple Barium-Alginate Membrane. *Diabetes* **2001**, *50*, 1698–1705.

(21) Vegas, A. J.; Veiseh, O.; Gürtler, M.; Millman, J. R.; Pagliuca, F. W.; Bader, A.

R.; Doloff, J. C.; Li, J.; Chen, M.; Olejnik, K.; *et al.* Long-Term Glycemic Control Using Polymer-Encapsulated Human Stem Cell – Derived Beta Cells in Immune-Competent Mice. **2016**, *22*.

(22) Scharp, David W, P. M. Encapsulated Islets for Diabetes Therapy: History, Current Progress, and Critical Issues Requiring Solution. *Adv. Drug Deliv. Rev.* **2014**, 35–73.

(23) Colton, C. K. Oxygen Supply to Encapsulated Therapeutic Cells. *Adv. Drug Deliv. Rev.* **2014**, *67–68*, 93–110.

(24) Weir, G. C. Islet Encapsulation: Advances and Obstacles. *Diabetologia* **2013**, *56*, 1458–1461.

(25) Bernards, D. a; Desai, T. a. Nanotemplating of Biodegradable Polymer Membranes for Constant-Rate Drug Delivery. *Adv. Mater.* **2010**, *22*, 2358–2362.

(26) Nyitray, C. E.; Chang, R.; Faleo, G.; Lance, K. D.; Bernards, D. A.; Tang, Q.; Desai, T. A. Polycaprolactone Thin-Film. *ACS Nano* **2015**, *9*, 5675–5682.

(27) Chroboczek, H.; Le, J.; Rubinjll, B. Y.; Yips, Y. K.; Naglersii, C. Three Molecular Weight Forms of Natural Human Interferon- ? Revealed by Immunoprecipitation with Monoclonal Antibody *. **1984**, *259*, 4301–4304.

(28) B. Beutler, D. Greenwald, J.D. Hulmes, M.Chang, Y.-C.E. Pan, J. Mathiason, R. U. & A. C. Identity of Tumour Necrosis Factor and the Macrophage-Secreted Factor Cachectin. *Nature* **1985**, *316*, 552–554.

(29) Hailey, K. L. The Expanding Folding/functional Landscape of the Interleukin-1 Family. *UC San Diego Electron. Theses Diss.* **2010**.

(30) Woodruff, M. A.; Hutmacher, D. W. The Return of a Forgotten polymer—Polycaprolactone in the 21st Century. *Prog. Polym. Sci.* **2010**, *35*, 1217–1256.

(31) Yuan, S.; Xiong, G.; Wang, X.; Zhang, S.; Choong, C. Surface Modification of Polycaprolactone Substrates Using Collagen-Conjugated Poly(methacrylic Acid) Brushes for the Regulation of Cell Proliferation and Endothelialisation. *J. Mater. Chem.* **2012**, *22*, 13039.

(32) Labet, M.; Thielemans, W. Synthesis of Polycaprolactone : A Review W. **2009**, 3484–3504.

(33) Hamilton, R. G.; Ph, D.; Abmli, D. The Human IgG Subclasses. **2001**.

(34) Itkin-ansari, P.; Levine, F. Cell-Based Therapies for Diabetes : Progress towards a Transplantable Human Cell Line Article in Annals of the New York Academy of Sciences · November 2003. **2003**.

(35) Fleury, J.; Siawaya, D.; Roberts, T.; Babb, C.; Black, G.; Golakai, H. J.; Bapela, N. B.; Hoal, E.; Parida, S.; Helden, P. Van. An Evaluation of Commercial Fluorescent Bead-Based Luminex Cytokine Assays. **2008**, *3*, 1–12.

(36) Pagliuca, F. W.; Millman, J. R.; Gürtler, M.; Segel, M.; Van Dervort, A.; Ryu, J. H.; Peterson, Q. P.; Greiner, D.; Melton, D. A. Generation of Functional Human Pancreatic β Cells In Vitro. *Cell* **2014**, *159*, 428–439.

(37) Micallef, S. J.; Li, X.; Schiesser, J. V; Hirst, C. E.; Yu, Q. C.; Lim, S. M. INS GFP / W Human Embryonic Stem Cells Facilitate Isolation of in Vitro Derived Insulin-Producing Cells. **2012**, 694–706.

(38) Taylor, B. L.; Liu, F.-F.; Sander, M. Nkx6.1 Is Essential for Maintaining the Functional State of Pancreatic Beta Cells. *Cell Rep.* **2013**, *4*, 1262–1275.

(39) Shih, H. P.; Seymour, P. A.; Patel, N. A.; Yeo, G. W.; Magnuson, M. A.; Sander, M.; Shih, H. P.; Seymour, P. A.; Patel, N. A.; Xie, R.; *et al.* Article A Gene Regulatory Network Cooperatively Controlled by Pdx1 and Sox9 Governs Lineage Allocation of Foregut Progenitor Cells Article A Gene Regulatory Network Cooperatively Controlled by Pdx1 and Sox9 Governs Lineage Allocation of Foregut Progenitor Cells. *CellReports* **2015**, *13*, 326–336.

(40) Krishnan, R.; Alexander, M.; Robles, L.; Iii, C. E. F.; Lakey, J. R. T. Islet and Stem Cell Encapsulation for Clinical Transplantation. **2014**, 84–101.

(41) Anderson, J. M.; Rodriguez, A.; Chang, D. T. Foreign Body Reaction to Biomaterials. *Semin Immunol.* **2008**, *20*, 86–100.

(42) Brown, B. N.; Ratner, B. D.; Goodman, S. B.; Amar, S.; Badylak, S. F. Macrophage Polarization: An Opportunity for Improved Outcomes in Biomaterials and Regenerative Medicine. *Biomaterials* **2012**, *33*, 3792–3802.

(43) Hentze, H.; Loong, P.; Tein, S.; Phillips, B. W.; Putti, T. C.; Dunn, N. R. Teratoma Formation by Human Embryonic Stem Cells : Evaluation of

Essential Parameters for Future Safety Studies. *Stem Cell Res.* **2009**, *2*, 198–210.

(44) Szot, G. L.; Koudria, P.; Bluestone, J. A. Transplantation of Pancreatic Islets Into the Kidney Capsule of Diabetic Mice Preparation of Islets for Transplant (Tx) Closing / Revival of Mouse. **2007**, 2–3.

(45) Zhu, Z.; González, F.; Huangfu, D. *The iCRISPR Platform for Rapid Genome Editing in Human Pluripotent Stem Cells*; 2014; Vol. 546.

(46) Characterization of the Ovalbumin-Specific TCR Transgenic Line OT-I : MHC Elements for Positive and Negative Selection. **2000**, 110–117.

(47) Li, D.; Yuan, Y.; Tu, H.; Liang, Q.; Dai, L. A Protocol for Islet Isolation from Mouse Pancreas. *Nat. Protoc.* **2009**, *4*, 1649–1652.

(48) Bruin, J. E.; Rezania, A.; Xu, J.; Narayan, K.; Fox, J. K.; O'Neil, J. J.; Kieffer, T. J. Maturation and Function of Human Embryonic Stem Cell-Derived Pancreatic Progenitors in Macroencapsulation Devices Following Transplant into Mice. *Diabetologia* **2013**, *56*, 1987–1998.

(49) Thompson, E. D.; Enriquez, H. L.; Fu, Y.; Engelhard, V. H. Tumor Masses Support Naive T Cell Infiltration , Activation , and Differentiation into Effectors. **2010**, *207*, 1791–1804.

II. Macroporous synthetic 3D polymer scaffolds for cell therapy in type 1 diabetes

A. ABSTRACT

Islet transplantation is a clinically proven therapy for diabetics to achieve insulin independence. However, current transplantation sites are either difficult to access or suboptimal in supporting the survival and function of transplanted islets. In this study, we demonstrate the use of a novel synthetic polymer matrix to remodel the microenvironment of the islet graft site in order to improve the success rate of islet transplantation procedures. Through in vitro studies, we characterize the maximal packing density of islets within the scaffolds as well as glucose stimulated insulin secretion from islets. In vivo studies suggest that transplantation of polymer scaffold loaded with islets improves the viability of islets and is able to revert diabetes in a syngeneic diabetic animal model. Finally, we demonstrate a few immunomodulatory strategies that can be combined with a scaffold material to overcome immune mediated graft rejection.

B. INTRODUCTION

Type 1 diabetes is a disease characterized by immune mediated destruction of insulin producing cells in the pancreas[1]. By the time that patients are diagnosed with the disease, a substantial amount of beta-cell mass

is loss, resulting in insulin insufficiency[2]. Chronic hyperglycemia leads to a long list of comorbidities including diabetic nephropathy, diabetic retinopathy, peripheral nerve disease, and other vasculopathies[3]. Currently, patients remain dependent on insulin for the rest of their lives through regular injections of long and short acting insulin daily[2]. Islet transplantation is the only proven option for patients to demonstrate long term insulin independence[4]. However, islet transplantation procedures have diminished over the years due to donor shortage and the necessity of chronic systemic immune suppression[5]. Several groups have shown promising results in providing immune protection of donor cells from the recipient immune system in animal models[6–9]. There is a particular interest in the exploration and engineering of islet transplant sites to improve islet viability and surgical accessibility[10–13]. In this study, we propose an alternative strategy to deliver islet replacement therapy by utilizing a highly tunable synthetic polymer scaffold to remodel the microenvironment of the islet transplant site.

Our goal is to fabricate a scaffold in which islet cell clusters may be spatially dispersed throughout the volume to prevent over aggregation that could exacerbate core necrosis, then ultimately lead to cell death and graft failure. To achieve this, we have designed a microporous scaffold made up of a synthetic polycaprolactone polymer material with pore sizes ranging from 150 to 250 micrometers. The size range of pore size was fabricated to allow for

efficient infiltration and containment of islets which have an average diameter of 150 micrometers. Templated microwells measuring 500 micrometers were introduced onto the loading surface of the polymer scaffolds to improve the distribution of the seeded cells. The final matrix scaffold is porous and flexible and can be cut to customized shapes to adhere to the desired transplant site and environment.

In this study, we demonstrate the ability of a polymer scaffold to improve the microenvironmental niche necessary for adequate islet cell survival and function. Through a series of in vitro and in vivo experiments, we have shown that islet cells packed within the scaffold preserve their insulin secretion kinetics in response to glucose challenge. Moreover, islet-scaffold constructs transplanted into syngeneic diabetic mice were successful in lowering blood glucose. In summary, these studies provide promising evidence to support the further development of synthetic scaffolds for the delivery of cells in cell replacement therapy for diabetes.

C. METHODS

Laser Etched Acrylic Mold

A honeycomb tiled template composed of 500 micrometer circles spaced 50 micrometers apart was illustrated in adobe's illustrator software. The

illustration was imported into ULS Laser Cutter system at the UCSF Center for Advanced Technology to produced etched patterns in acrylic slabs measuring. The acrylic mold is approximately 4x2 inches with honeycomb pattern of 500 micrometer wells neatly patterned across the surface. The final acrylic slab was cleaned by sonicating in a beaker filled with deionized water and isopropryl alcohol (10% v/v).

Polydimethylsiloxane (PDMS) Negative Template Mold

Polydimethylsiloxane (Sylgard 184) was cast onto the laser etched acrylic mold. PDMS was crosslinked by adding 10% initiator solution and baked in 50C vacuum pressured oven overnight. The PDMS was then peeled from the acrylic mold to yield the final negative template mold.

3D polymer scaffold fabrication

3D polymer scaffolds were fabricated using polycaprolactone combined with a salt leaching method. Briefly, 80kDa polycaprolactone and 2kDa polyethylene glycol was dissolved in trifluoroethanol at a concentration of 100 mg/mL. The mixture polymer solution was sonicated for 30 minutes using a water bath sonicator to achieve a homogeneous solution. Salt was added to the polymer solution at 10g/mL and agitated to form a slurry. The polymer-salt slurry was then cast onto the PDMS negative template mold and allowed to dry in a

chemical hood overnight. The final polymer-salt-PDMS construct was submerged in a beaker filled with deionized water to allow the salt to leach out of the scaffold. The final polymer scaffold is then peeled off of the PDMS.

Glucose Stimulated Insulin Secretion

An automated perifusion (Biorep) was used to measure the insulin secretion kinetics of islets in response exposure to varying glucose concentration buffers. Free islets were loaded into the bioreactor chambers by first packing polyacrylamide beads into the chambers before depositing 100 islet clusters. Scaffolds were cut to fit the diameter of the bioreactor and pre-loaded with 100 islets before being inserted into the bioreactor chamber. The flow rate of the perifusion system was set to 100uL/min and perfusates from each bioreactor chamber was collected every 150 seconds in a 96 well plate. Finally, insulin concentrations from the perfusate were quantified using a commercial ELISA kit (Mercodia).

Surface Protein Conjugation

Fabricate a trilayer PCL film. Spin coat each layer at 500 rpm for 45s. Bottom layer: 10 mg/mL of PMPI – PCL in TFE. Add about 0.5 mL of mixture onto wafer. After spin coating, layer dries in under 1 minute. Middle layer: 100 mg/mL of PCL in TFE. Add about 2 mL of mixture onto wafer. After spin coating, layer dries in about 5 minutes. Top layer: 10 mg/mL of PMPI – PCL in

TFE. Add about 2 mL of mixture onto wafer. After spin coating, layer dries in 2-3 minutes.

Use Traut's reagent to thiol-activate EGFP. Prepare a stock solution of pH 8.0 PBS by adjusting pH 7 PBS by adding NaOH drop by drop. Add 3 mM EDTA. Dilute stock EGFP solution in pH 8.0 PBS, 3 mM EDTA buffer. Add Traut's reagent (diluted to 14 mM in water or PBS) so that [Traut's reagent] = 10 [GFP] (concentrations). Set for 1 hour at RT, keep covered. While reaction tube is incubating, equilibrate a desalting column using the pH 8.0 PBS, 3 mM EDTA buffer. Run reaction mixture through desalting column. Leave both maleimide-doped and control films overnight, adding 500 uL of the eGFP solutions. Keep covered and at RT on a shaker.

Quantification of Conjugated Protein

Measure fluorescence of films once taken out of solution using excitation 485 nm, emission 515 nm. Using a standard curve of serial dilution of eGFP, the mass can be calculated.

Desorption of Surface Protein

Protein adsorbed material was immersed in 1% SDS for 2 hours on a shaker at room temperature. Measurement of fluorescent protein on films was

performed using a fluorimeter. Films were sonicated in 1% SDS for 5 minutes twice. Quantification of protein mass on surface was performed using a BCA assay on both desorption buffer fractions as well as directly on the film.

Cell Culture

Isolation of mouse islets was performed as described¹⁴¹⁴¹³¹²¹⁰⁹⁷⁶⁵⁴⁴³²².

Islets and MIN6 cells were cultured in RPMI 1640 supplemented with 10%(v/v) fetal bovine serum. Undifferentiated Mel1$^{INS\text{-}GFP}$ cells[15] were maintained on mouse embryo fibroblast feeder layers (Milli- pore) in hESC media as described[16]. Suspension- based direct differentiations to generate hES-βC were carried out as described[17] with improvements to the last stage based on published reports[18,19].

Gene targeting of Mel1$^{INS\text{-}GFP}$ cells

To generate a cell line that expresses a constitutive firefly luciferase gene we employed recently published gene targeting approach of the insulated human AAVS1 loci employing TALENs. Briefly, we amplified a 6332 bp DNA piece containing all bacterial components, both homologies to the human AAVS1 loci, as well as the puromycin resistance gene from the Puro-Cas9 donor

plasmid (Addgene #58409) and cloned a fragment consisting of a peptide cleavage site T2A, followed by the firefly luciferase gene and a poly A sequence in, to re-circulate the DNA piece. The resulting plasmid, termed Puro-T2A-Luc donor, was sequence verified by sanger sequencing. Confluent Mel1$^{INS-GFP}$ were dissociated to single cells and approximately 8,0x106 cells were mixed with 5ug of each of the TALEN plasmids and 20ug of the Puro-T2A-Luc donor in a 0,4cm gap electro-cuvette (Biorad). Cells were electroporated using a GenePulser (Biorad) using an exponential decay with 250V and 500uF settings. Targeted cells were plated on DR4 resistant MEFs and clones were selected with 0.5ug/ml Puromycin for 4 days. After 11-12 days, individual clones were manually picked and expanded before freeze down and genomic DNA analysis. gDNA was analyzed with primers for WT and correct Puro integration. WT/Puro Forward: CCG GAA CTC TGC CCT CTA AC, WT Reverse: AGA TGG CTC CAG GAA ATG GG, Puro Reverse: GTG GGC TTG TAC TCG GTC AT. Mel1$^{INS-GFP,AAVS1-Luc}$ line #3 was used for direct differentiation experiments.

Mice

NOD.Cg-Prkdcscid Il2rgtm1Wjl/SzJ mice (NSG) and C57BL/6J mice were obtained from Jackson Laboratories. Mice used in this study were maintained according to protocols approved by the University of California, San Francisco Committee on Laboratory Animal Resource Center. For kidney capsule grafts, approximately 2.0 × 10^6 hESC-differentiated cells in clusters were transplanted

as described[20]. For subcutaneous grafts, approximately 2.0×10^6 hESC-differentiated cell sin clusters were transplanted on the left dorsal aspect of the animal. For epidydimal fat pad grafts with and without scaffolds, a small incision was made to access the epidydimal fat pad and approximately 200 islet clusters were inserted before suturing up the animal.

In vivo Bioluminescence Imaging

Survival of cells in vivo was assessed by monitoring luciferase activity using a Xenogene IVIS 200 imaging system (PerkinElmer). The animals transplanted with hSC-βC cells were injected IP with D-luciferin solution (Goldbio, St. Louis,MO) at the dose of 150 mg/kg 5 min before imaging to capture the peak in bioluminescent intensity. The mice were anesthetized with an isoflurane mixture (2% in 98% O2) and imaged by using a Xenogen IVIS 200 imaging system. Bioluminescence images were acquired for 3 min and then analyzed using the Living Image analysis software (Xenogen, Alameda, CA). Regions of interest (ROI) were centered over the bioluminescence regions. Photons were counted within the ROI over the acquisition time. Adherence to the same imaging protocol ensured consistent signal detection on different days of in vivo imaging.

D. RESULTS

Fabrication of templated 3D polymer scaffold

We designed a 3D polymer scaffold to facilitate the transplantation of islets in a manner that permits optimal packing of islets with better spatial distribution. The scaffolds have been designed with stochastic macroporous structures that serve the function of allowing islets to embed within as well as the ingrowth of blood vessels to vascularize the islets. By transplanting islets seeded on an organized matrix scaffold instead of direct delivery free islets, we hypothesize that we are able to achieve a more functional graft capable of reversing diabetes.

In order to produce a scaffold that better distributes seeded islets spatially with minimal aggregation, we fabricated precise microwell structures onto one surface of the polymer scaffold. Microwells measuring 500 microns in diameter were first etched into an acrylic mold using a laser cutter (**Fig 2-1a**). Polydimethylsiloxane (PDMS) was then cast on to the templated acrylic and crosslinked to produce a negative mold consisting of 500 micron posts (**Fig 2-1b**). Polycaprolactone and polyethylene glycol was dissolved in trifluoroethanol combined with potassium chloride salt crystals to form the polymer – porogen slurry (**Fig 2-2**). Salt particles measuring between 150 to 250 microns were selected to match the approximate size of isolated mouse islets. The slurry was mixed thoroughly by agitation before cast onto the PDMS

negative mold and allowed to dry overnight. Finally, porogens were leached out of the polymer scaffold using deionized water (**Fig 2-3**). The final polymer scaffold is approximately 1mm thick consisting of 500 micron wells with interconnected pores measuring 150 to 250 microns.

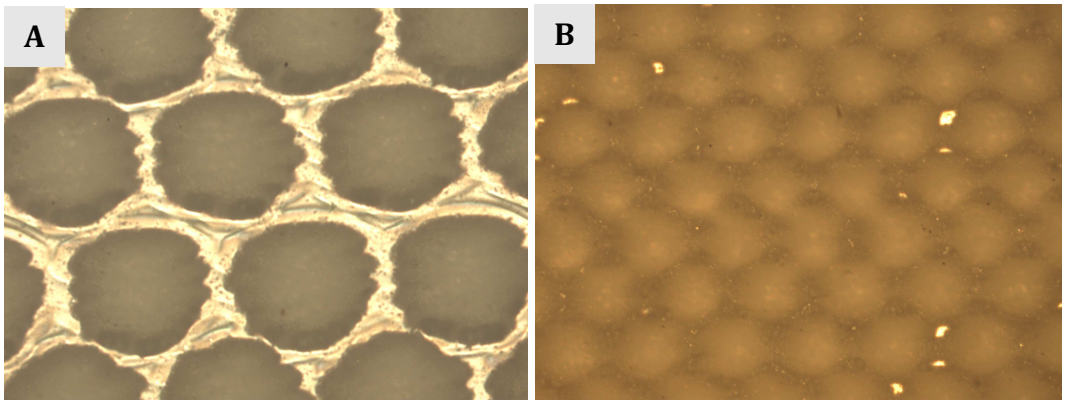

Figure 2.1 Template Fabrication for polymer scaffold. a, templated acrylic mold consisting of 500 micron wells with 50 micron spacing textured in a honeycomb pattern following laser cutting. **b,** templated PDMS negative mold consisting of 500 micron posts with 50 micron spacing textured in honeycomb pattern.

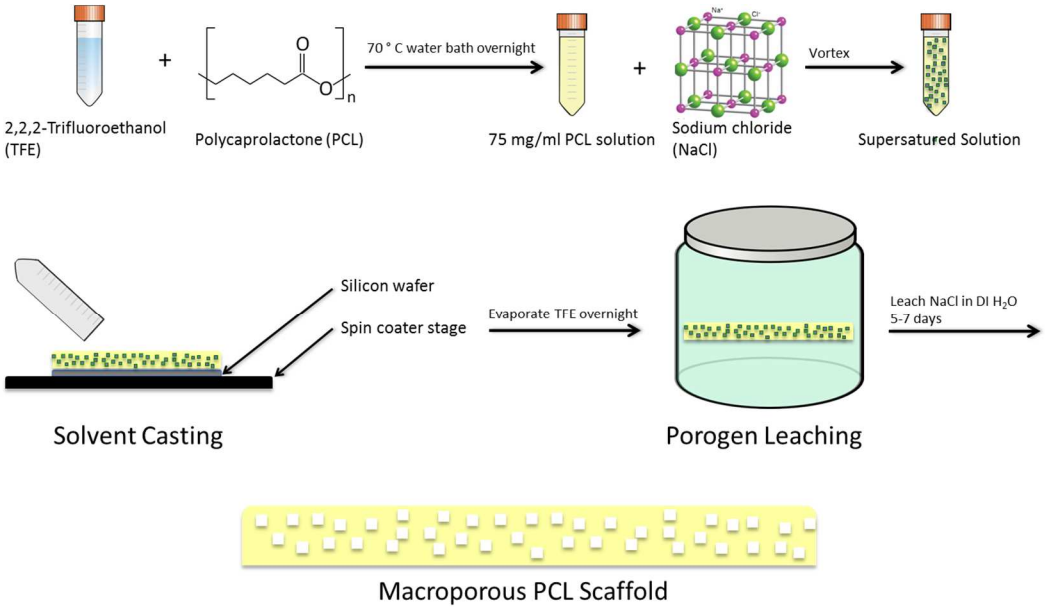

Figure 2.2 – Fabrication scheme for polymer – porogen slurry.

Polycaprolactone and polyethyelene glycol are dissolved in trifluoroethanol in a 70C water bath overnight. Sodium chloride particles were then introduced to the homogenous polymer mixture to yield a supersaturated polymer-porogen slurry. The slurry was agitated to mix thoroughly before casting onto templated silicon PDMS substrate and allowed to dry overnight. Porogen leaching was performed in deionized water for 5 days to fully remove the salt.

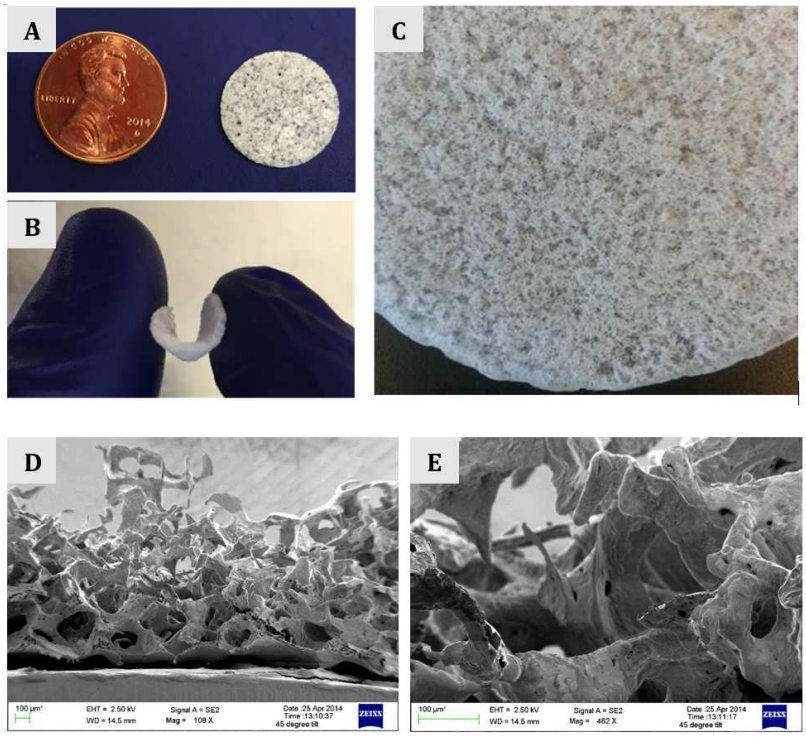

Figure 2.3 – polycaprolactone scaffold for cell seeding. a, gross image of polymer scaffold cut to a circular wafer. **b,** gross image of polymer scaffold showing flexibility of material. **c,** scaffold image showing highly porous architecture within the matrix. **d,** scanning electron micrograph of pores within the polymer scaffold. **e,** scanning electron microscopy image of cross section of polymer scaffold showing thickness and pores within matrix.

Cell loading capacity and viability within polymer scaffold

One of the key considerations for an optimal scaffold for islet transplantation is the ability the load or pack sufficient islets into the matrix. Packing density needs to be controlled such that the islets do not over-aggregate to cause core necrosis yet can be sufficiently condensed so that enough islets can be loaded

in a reasonable surface area to achieve a therapeutic effect. As an initial step to validate the ability of PCL macroporous scaffolds to retain islets, we seeding single MIN6 cells onto the collagen, laminin, or collagen and laminin coated scaffolds at increasingly seeding densities. The cell-scaffold constructs were cultured overnight in complete cell culture medium before being transferred into new polystyrene wells and quantified for the amount of cell retaining. Our experiment results show that we can consistently retain approximately 60% of the seeded cells regardless of initial seeding density or surface protein coating (**Fig 2.4a)**. These results indicate that we can sufficient pack the scaffolds with enough beta cells to reach a therapeutic effect in vivo. However, seeding of single cells may not fully recapitulate the effect of loading islets or beta-like stem cell clusters within the scaffold.

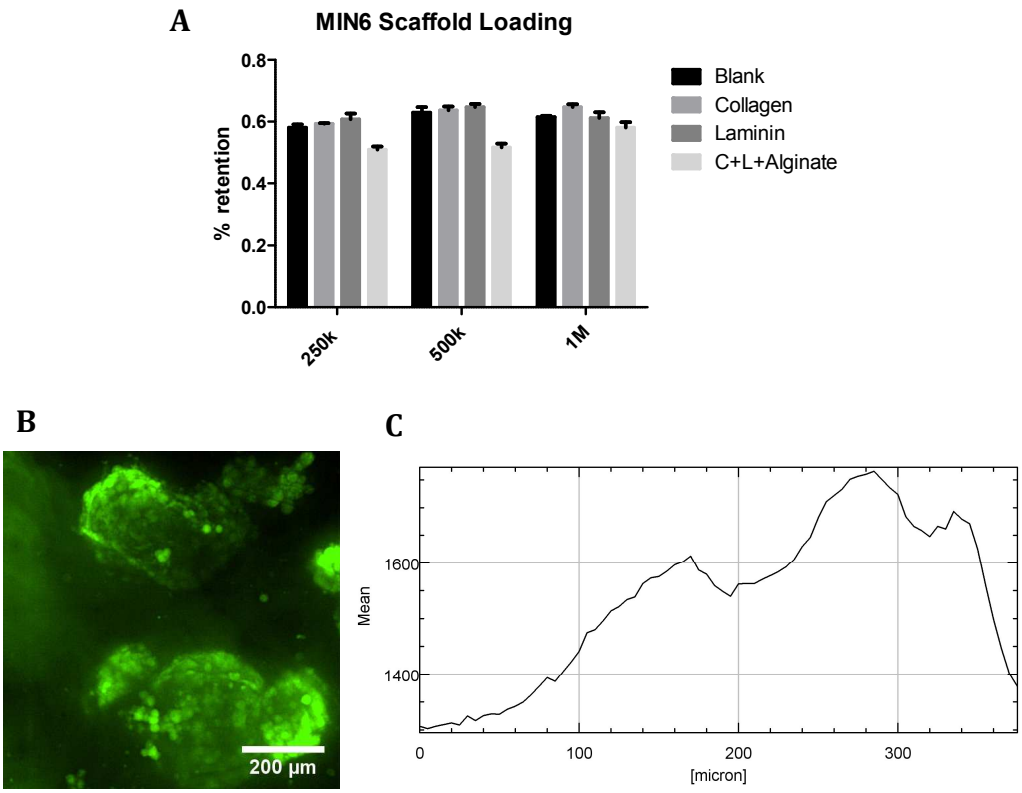

Figure 2.4 - **Characterization of scaffold retention of single beta cells and islet clusters**. **a,** MIN6 cells loaded onto scaffolds measuring 0.36 cm^2 in area and 1mm in thickness at 2.5 x 10^5, 5 x 10^5, and 10^6 cells per scaffold. Scaffolds were also coated with either collagen, laminin, or collagen and laminin. Percent retention was measured by fraction of cells retained on scaffold after being transferred into a new well. (n=6 per group) **b,** representative fluorescent confocal microscopy of 100 MIP-Luc islet clusters loaded within PCL scaffolds. **c,** mean fluorescent intensity (y-axis) as measured throughout the thickness of the entire scaffold (x-axis).

We proceeded to loading the scaffolds with islets engineered with a luciferase reporter driven by the mouse insulin promoter. In this experiment, scaffolds with loaded with 100 islets and imaged by confocal microscopy. Our results indicate that islets do indeed infiltrate throughout the fully thickness of the scaffold as opposed to being merely seeding on the top surface (**Fig. 2.4 a, b,c**). We hypothesize that the packing density of each scaffold can exceed the 100 islets we loaded. Packing efficiency is expected to fall as attempt to increase the packing density within the scaffold. To further investigate and characterize the maximum loading capacity of each scaffold, we seeded PLGA microparticles measuring 150 micrometer in diameter, similar to the average size of islets. Confocal microscopy of microparticle loaded scaffolds show infiltration throughout the z-axis or thickness of the matrix (**Fig 2.5a**). Moreoever, consistent with our hypothesis, the loading efficiency drops precipitously as we increase the loading density (**Fig 2.5b,c)**. We show that the loading capacity is maximized at approximately 300 islet clusters for the 1mm thick scaffold, and slightly higher at 350 islet clusters for the 1.5mm thick scaffold (**Fig 2.5b)**. With each attempt to load 50 additional cluster into the scaffold, loading efficiency also drops. A significant drop was observed when attempting to load up to 250 clusters and 350 clusters into the 1mm scaffolds respectively (**Fig 2.5c)**.

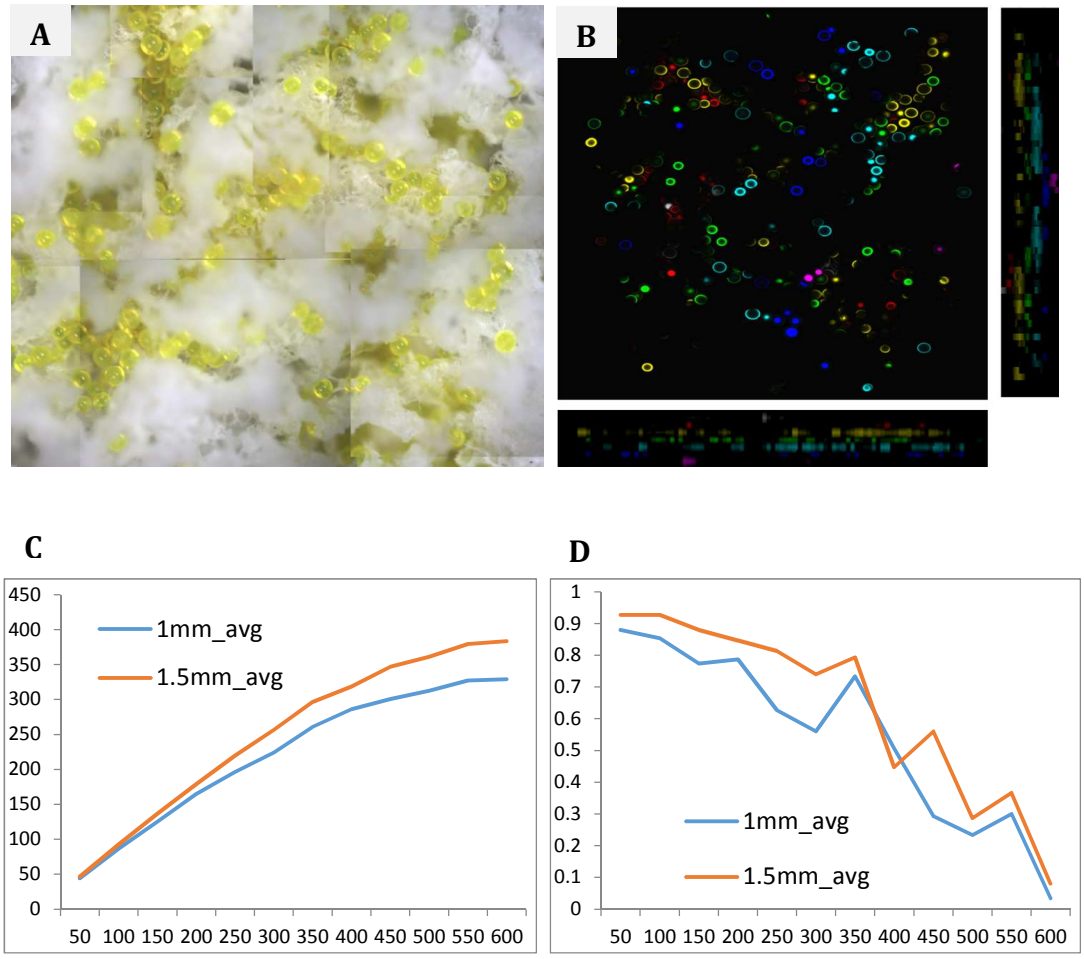

Figure 2.5 – Characterization of loading efficiency and capacity of PCL scaffolds. a, brightfield image of PLGA microsphere loaded into PCL scaffolds. **b**, z-stack composite image of fluorescence confocal microscopy of GFP labeled 150 micrometer PLGA microspheres loaded within scaffold. **b**, plot of intended microsphere count loaded (x-axis) and microsphere count retained on scaffold (y-axis) for scaffolds measuring 1mm and 1.5 mm in thickness respective. **c,** plot of retention efficiency of scaffolds with each successive attempt to load 50 additional microspheres. (n=4 per group)

Characterization of viability and function of cells loaded PCL scaffolds

The ability load scaffolds with single cells or clusters may not directly translate into cell viability and function within the new matrix environment. To investigate the viability of single cells in scaffold, we seeded mCherry – MIN6 cells onto PCL scaffolds or tissue culture treated plastic at 20,000 cells per $0.36cm^2$ area. Fluorescent intensity of mCherry cells were measured daily and we observed elevated cell proliferation on the PCL scaffolds (**Fig 2.6a**). PCL scaffolds through its 3D architecture may have significantly increased the surface area for Min6 cell adhesion compared to flat 2D tissue culture surfaces. We further assessed the function of mature primary mouse islets loaded in scaffolds coated with collagen, laminin, or blank. We loaded 50 islets in each scaffold or control and utilized an automated islet perifusion system to flow low and high glucose concentration buffer continuously through scaffolds a precise flow rates. Perfusate was collected every 2.5 minutes for each sample. Our experimental results suggest that uncoated scaffolds and collagen coated scaffolds performed non-inferiorly when compared to free islets. More specifically, there was no delay in insulin secretion kinetics when islets were transitioned in between different glucose concentration buffers **(Fig. 2.6b)**. Although it is worth noting that islets seeded on scaffolds did not produce an expected biphasic insulin secretion response when stimulated under high glucose media as seen in the free islet controls **(Fig 2.6b**). Nevertheless, the

results of this study confirmed that glucose and insulin diffusion kinetics were uninhibited by the scaffold material when compared to free islets.

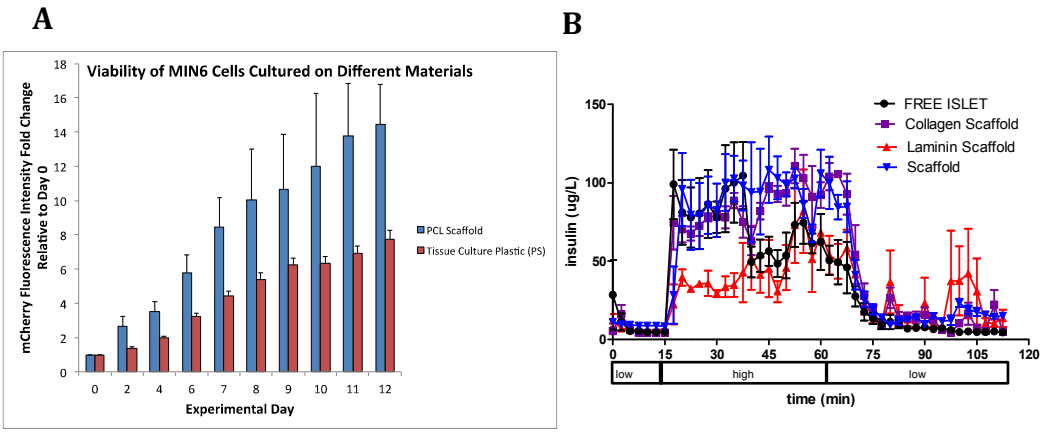

Figure 2.6 – Characterization of viability and insulin secretion function in cell and islet loaded scaffolds. a, fluorescent intensity measured from mCherry expressing Min6 cells loaded on tissue culture plastic or PCL scaffold. (n=4 per group) **b,** Insulin secretion kinetics in response to low (2mM), high (20mM), and low (2mM) glucose perifusion challenge for free islets, and islets seeded on uncoated, collagen coated, and laminin coated PCL scaffolds. (n=3 per group)

Characterization of scaffold in vivo transplants and reversal of diabetes

Although scaffolds loaded with islets have been demonstrated favorable loading capacity and glucose stimulated insulin secretion kinetics, the translation to in vivo therapeutic response is still unclear. With an islet-scaffold construct, we seek to access a transplantation site in a minimally invasive manner such as the subcutaneous space or epididymal fatpad that

may have been unfavorable for free islets to survive and function. To further elucidate the therapeutic potential of our islet-scaffold construct and demonstrate that it may be superior to loading free islets, we performed in vivo transplants. First, stem cell derived beta-like cell clusters consisting of pancreatic progenitors and mature-beta like cells were pre-seeded onto scaffolds and transplanted into the subcutaneous space in NSG mice (**Fig 2.7 a-d**). The results show that cells infiltrated throughout the entire volume of the scaffolds and luciferase reporter indicate viable cells both in vitro and in vivo on day of transplant and also 30 days post-transplant. Luciferase based in vivo images suggests that viability signal is stable throughout the course of 30 days which compares favorably to historical free islet only controls transplanted subcutaneously or in the kidney capsule where the bioluminescence intensity is reduced by more than 95%, and 80% respectively by day 20 (**Fig 2.7 e,f**). These results are promising evidence that islet cells seeded onto PCL scaffolds may offer the cells improved survival benefit when transplanted subcutaneously. To assess whether this improvement in cell survival translates into added therapeutic efficacy, we transplanted mature mouse islets isolated from wildtype C57B6/J mice into the epidydimal fat pads of syngeneic diabetic mice. Our experimental results indicate that islets transplanted with or without scaffolds were both able to reverse diabetes within 3 days of transplantation measured by blood glucose under 250 mg/dL. However, in animals with islets transplanted without scaffolds, blood glucose rose after a

week and failed to continue to control blood glucose levels. This can be explained by the possibility that substantial beta cell mass has been lost due to cell death following one week of transplantation. In contrast, diabetic mice that received islets in scaffold transplants continued to have controlled blood glucose levels under 250 mg/dL up to 30 days after transplantation (**Fig 2.7g**). We show in this series of studies that PCL scaffolds may convert previously unfavorable transplant sites into more advantageous microenvironments that offer improved cell survival and therapeutic efficacy in controlling elevated blood glucose.

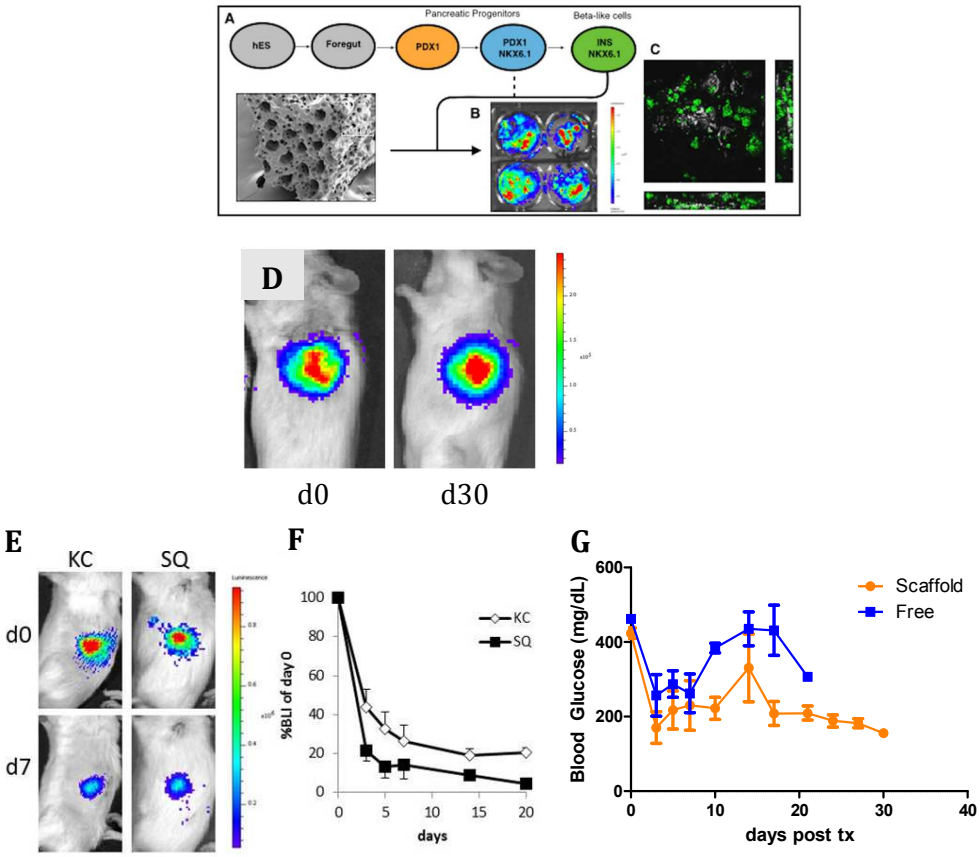

Figure 2.7 – In vivo efficacy of stem cell derived beta cell clusters and mature mouse islets seeded on scaffolds. a, schematic illustration of differentiation schedule of stem cell derived beta cells and stage at which cells were loaded into scaffolds. **b,** bioluminescent imaging showing loaded stem cells are viable within scaffolds. **c**, fluorescent microscopy of stem cells transduced with GFP reporter driven off insulin promotor within scaffolds. **d**, In vivo luciferase bioluminescent image of stem-cell scaffold construct on day 0 and 30 after subcutaneous transplant into NSG mice. **e**, Bioluminescent image of stem cells transplanted without scaffolds in the subcutaneous space and in the kidney capsule of NSG mice on day 0 and 7 following transplantation. **f,** quantification bioluminescent intensity of subcutaneous and kidney capsule transplants up to day 20. **g**, glucose levels of STZ induced diabetic B6 mice that received epidydimal transplants with syngeneic islets with or without scaffolds. (n=3 per group)

Immunomodulatory materials to deliver local immune suppression

The macroporous design of the PCL scaffold provides the benefit of uninhibited insulin secretion and infiltration of blood vessels to support engrafted cells. However, it does not address the issue of graft rejection by the host immune response. In Chapter 1, we illustrated an immunoprotective approach to thwart immune mediated rejection. Here, we describe another approach that entails reprogramming the local immune environment through

the release of drugs to inhibit immune response locally. Rapamycin is an mTOR inhibitor that inhibits T cell proliferation and function. As a hydrophobic small molecule drug, it can be fully intercalated within the polymer matrix of polycaprolactone and dissolved within organic solvents. We demonstrate controlled continuous release of rapamycin intercalated into a bulk PCL ring (**Fig 2.8a**). In addition, antibodies may be conjugated onto the surface of polycaprolactone scaffolds using NHSS-EDC chemistry (**Fig 2.8b)**. Neutralizing antibodies against specific proinflammatory cytokines such as interferon-gamma or tumor necrosis factor – alpha may be immobilized onto the scaffold surface. This provides a plausible alternative to complete immune-isolation by reprogramming the local immune environment through local immune suppression. By combining immunomodulatory techniques with the highly favorable local microenvironment provided by scaffolds for cell transplants, we strive to achieve a therapeutically practical product for clinical use.

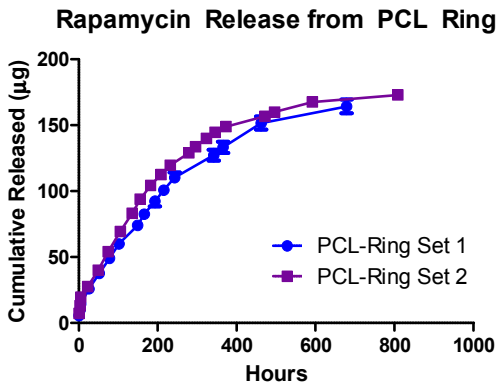

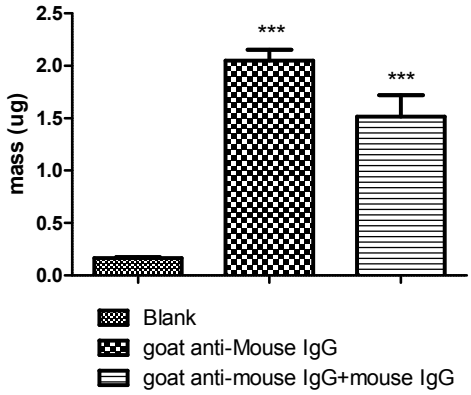

Figure 2.8 Local release of Rapamycin from nonporous PCL ring. a, Rapamycin mixed within a polymer matrix is released in a controlled and continuous fashion over the course of a month. Plot shows two sets of samples. (n=2 per group). **b,** quantification of mass from anti-mouse IgG conjugated onto polycaprolactone surfaces using NHSS-EDC chemistry.

E. DISCUSSION

In this study, we demonstrate fabrication of novel polymer scaffold with highly controlled templated construct for the application of supporting seeded cells in cell replacement therapy for diabetes. We produced a highly porous and flexible polymer scaffold matrix designed specifically for the infiltration and retention of pancreatic islets. Our studies demonstrate that islets can be reliably packed within scaffolds at high packing densities that extend throughout the thickness of the material. Cell viability and functional studies suggest that the material is compatible with cell viability and the key function of glucose stimulated insulin secretion by islets is not negatively impacted by the scaffold. In our animal studies, we show promising evidence that PCL scaffolds promote cell viability in transplant sites that may be naturally suboptimal. Both stem cell derived beta-cell clusters and primary mouse islets can be packed within a scaffold and transplanted into mouse recipients. Transplanted cells are not only viable but also function as they show therapeutic efficacy in correcting high glucose in diabetic animal models.

Finally, we illustrate the ability to elute immune suppressive drugs from the matrix with the goal of achieving local immune modulation to prevent graft rejection by the host immune system.

Future studies may involve combining multiple drug delivery strategies within this polymer scaffold to achieve robust immune modulation in vivo. For example, the neutralizing of proinflammatory cytokines, the enrichment of regulatory T cells, and the inactivation of primed effector T cells at the site of scaffold graft are all interesting strategies. The successful engineering of an immunomodulatory scaffold may provide the most direct path forward for stem cell replacement therapy for near term clinical application in diabetes.

F. REFERENCES

(1) Lehuen, A.; Diana, J.; Zaccone, P.; Cooke, A. Immune Cell Crosstalk in Type 1 Diabetes. *Nat. Rev. Immunol.* **2010**, *10*, 501–513.

(2) Belle, T. O. M. L. V. A. N.; Coppieters, K. E. N. T.; Herrath, M. G. V. O. N. Type 1 Diabetes : Etiology , Immunology , and Therapeutic Strategies. **2011**, 79–118.

(3) Melendez-ramirez, L. Y.; Cefalu, W. T.; Richards, R. J. Complications of Type 1 Diabetes. *Endocrinol. Metab. Clin. NA* **2010**, *39*, 625–640.

(4) Citr, T. 2007 Update on Allogeneic Islet Transplantation from the Collaborative Islet Transplant Registry (CITR). *Cell Transplant.* **2009**, *18*,

753–767.

(5) Robertson, R. P. Islet Transplantation as a Treatment for Diabetes — A Work in Progress. **2004**, 694–705.

(6) Beck, J.; Angus, R.; Madsen, B.; Britt, D.; Vernon, B.; Nguyen, K. T. Islet Encapsulation: Strategies to Enhance Islet Cell Functions. *Tissue Eng.* **2007**, *13*, 589–599.

(7) Desai, T.; Shea, L. D. Advances in Islet Encapsulation Technologies. *Nat. Publ. Gr.* **2016**.

(8) Buder, B.; Alexander, M.; Krishnan, R.; Chapman, D. W.; Lakey, J. R. Encapsulated Islet Transplantation: Strategies and Clinical Trials. *Immune Netw.* **2013**, *13*, 235–239.

(9) Vegas, A. J.; Veiseh, O.; Gürtler, M.; Millman, J. R.; Pagliuca, F. W.; Bader, A. R.; Doloff, J. C.; Li, J.; Chen, M.; Olejnik, K.; *et al.* Long-Term Glycemic Control Using Polymer-Encapsulated Human Stem Cell–derived Beta Cells in Immune-Competent Mice. *Nat. Med.* **2016**.

(10) Cantarelli, E.; Piemonti, L. Alternative Transplantation Sites for Pancreatic Islet Grafts. *Curr. Diab. Rep.* **2011**, *11*, 364–374.

(11) Kim, J. S.; Lim, J. H.; Nam, H. Y.; Lim, H. J.; Shin, J. S.; Shin, J. Y.; Ryu, J. H.; Kim, K.; Kwon, I. C.; Jin, S. M.; *et al.* In Situ Application of Hydrogel-Type Fibrin-Islet Composite Optimized for Rapid Glycemic Control by Subcutaneous Xenogeneic Porcine Islet Transplantation. *J. Control. Release* **2012**, *162*, 382–390.

(12) Carlsson, P.-O. Influence of Microenvironment on Engraftment of Transplanted β-Cells. *Ups. J. Med. Sci.* **2011**, *116*, 1–7.

(13) Luan, N. M.; Iwata, H. Long-Term Allogeneic Islet Graft Survival in Prevascularized Subcutaneous Sites without Immunosuppressive Treatment. *Am. J. Transplant* **2014**, *14*, 1533–1542.

(14) Li, D.; Yuan, Y.; Tu, H.; Liang, Q.; Dai, L. A Protocol for Islet Isolation from Mouse Pancreas. *Nat. Protoc.* **2009**, *4*, 1649–1652.

(15) Micallef, S. J.; Li, X.; Schiesser, J. V; Hirst, C. E.; Yu, Q. C.; Lim, S. M. INS GFP / W Human Embryonic Stem Cells Facilitate Isolation of in Vitro Derived Insulin-Producing Cells. **2012**, 694–706.

(16) Guo, T.; Landsman, L.; Li, N.; Hebrok, M. Factors Expressed by Murine Embryonic Pancreatic Mesenchyme Enhance Generation of Insulin-Producing Cells from hESCs. *Diabetes* **2013**, *62*, 1581–1592.

(17) Russ, H. A.; Parent, A. V; Ringler, J. J.; Hennings, T. G.; Nair, G. G.; Shveygert, M.; Guo, T.; Puri, S.; Haataja, L.; Cirulli, V.; *et al.* Controlled Induction of Human Pancreatic Progenitors Produces Functional Beta-like Cells in Vitro. **2015**, *34*, 1759–1772.

(18) Bruin, J. E.; Rezania, A.; Xu, J.; Narayan, K.; Fox, J. K.; O'Neil, J. J.; Kieffer, T. J. Maturation and Function of Human Embryonic Stem Cell-Derived Pancreatic Progenitors in Macroencapsulation Devices Following Transplant into Mice. *Diabetologia* **2013**, *56*, 1987–1998.

(19) Pagliuca, F. W.; Millman, J. R.; Gürtler, M.; Segel, M.; Van Dervort, A.; Ryu,

J. H.; Peterson, Q. P.; Greiner, D.; Melton, D. A. Generation of Functional Human Pancreatic β Cells In Vitro. *Cell* **2014**, *159*, 428–439.

(20) Szot, G. L.; Koudria, P.; Bluestone, J. A. Transplantation of Pancreatic Islets Into the Kidney Capsule of Diabetic Mice Preparation of Islets for Transplant (Tx) Closing / Revival of Mouse. **2007**, 2–3.

III.Immuno-engineered oncolytic virus inspired nanoparticle tumor vaccines

A. ABSTRACT

Immunotherapy has garnished much attention recently brought on by the compelling clinical efficacy we are seeing in advanced melanoma patients treated with checkpoint inhibitors such as ipilimumab and nivolumab targeting CTLA-4 and PD-1. Since the FDA's initial approval of these drugs for melanoma, checkpoint inhibitor immunotherapy has been subsequently approved for other types of cancer including non small cell lung carcinoma and renal cell carcinoma. Scientists in the field of immunotherapy have also achieved success in cellular therapeutics using chimeric antigen receptor engineered T cells (CAR-Ts) that target CD19 to treat acute lymphocytic leukemia. A recent phase 3 clinical trial demonstrating improved durable response rate for patients with advanced melanoma treated with a modified herpes simplex virus type 1(HSV-1) encoding GM-CSF led to the approval of

talimogene laherparepvec (T-VEC; Amgen) by the FDA[1]. The proliferation of immunotherapy approaches has provided us essential arsenal in our battle against cancer. Although these approaches have proven to demonstrate miraculous efficacy for a subset of patients, we strive to achieve more widespread benefit for more of our patients. Furthermore, the manufacturing cost and toxicities associated with some of these immunotherapy approaches are significant barriers that need to be overcome in order for us to deliver safer and more potent immunotherapies to more cancer patients in need. Our goal is to provide a cancer immunotherapy using immune stimulating nanoparticles that can be used to treat more widespread types of primary tumors and distance metastases with lower systemic toxicities at significantly lower cost for manufacturing, storage and delivery. In this study, we demonstrate a cocktail of immune adjuvants and tumor antigen co-encapsulated within a polymeric nanoparticle can effectively inhibit tumor growth in a syngeneic melanoma tumor model.

B. INTRODUCTION

Oncolytic viruses promote anti-tumor responses through direct tumor lysis and induction of systemic anti-tumor immunity. A recent phase 3 clinical trial demonstrating improved durable response rate for patients with advanced melanoma treated with a modified herpes simplex virus type 1(HSV-1)

encoding GM-CSF led to the approval of talimogene laherparepvec (T-VEC; Amgen) by the FDA[1].

The release of tumor associated antigens, local cytokines, cellular danger-associated molecular pattern signals (DAMPS), and pathogen-associated molecular patterns (PAMP)s, promotes the maturation of antigen-presenting cells (APCs) and subsequent activation of antigen-specific $CD4^+$ and $CD8^+$ T cell responses that mediate tumor regression at distance sites[2]. Systemic anti-tumor immune response induced by oncolytic viruses remains poorly understood but is thought to be related to viral components that elicit danger signals through the engagement of PAMPs with pattern recognition receptors (PRRs). PAMPs may include elements of viral capsids, DNA, RNA, and viral protein products that bind to Toll-like-receptors (TLRs), cytosolic nucleotide sensor stimulator of IFN genes (STING), or retinoic acid inducible gene 1 (RIG-1) to induce downstream activation of the JAK-STAT pathway to trigger local IFN release[2]. Type 1 IFNs stimulate antigen presenting cells (APCs), $CD8^+$ T cells and NK cells to orchestrate innate and adaptive anti-tumor immunity[3].

We aim to dissect the role of TLR, STING, and RIG-1 ligands as immune adjuvants in promoting systemic anti-tumor responses following local intratumoral injection. By locally delivering poly(lactic-co-glycolic acid) (PLGA) nanoparticles encapsulating tumor associated antigens and key viral-

related immune adjuvants, we hypothesize that we may further dissect mechanisms in inducing systemic anti-tumor immunity seen in oncolytic virotherapy and facilitate future rational design of immunotherapies to induce anti-tumor immunity.

Cytosolic nucleotide sensor stimulator of IFN genes (STING) localizes to the endoplasmic reticulum and senses cyclic dinucleotides (CDNs) to induce potent type 1 IFN secretions. STING is expressed in T cells, macrophages and dendritic cells (DCs), and can be stimulated by DNA viruses and bacteria. It has been shown that endogenous STING pathway activation within the tumor microenvironment(TME) induces local T cell priming, mediates regression of both locally treated tumor and distant metastases, and establishes T cell memory[4,5]. The STING pathway is also responsible for radiation-induced and spontaneous natural antitumor responses as STING-deficient mice fail to generate robust anti-tumor T cell response against melanoma[6,7]. Interestingly, STING is required for the stimulation of T cell responses by checkpoint inhibitors[8]. Local controlled delivery of STING agonists to the TME may further potentiate anti-tumor immunity by improving activation and priming of DCs and T cells.

TLR9 is activated by the binding of internalized dsDNA onligonucleotides that contain unmethylated CG dinucleotides (CpG ODN) 21 bases long[9,10]. TLR9 is

mainly expressed in plasmacytoid DCs (pDCs) and B cells[11]. TLR9 agonists activate pDCs to secrete type I IFN and upregulates CD80, CD86 costimulatory molecules, as well as trigger activation of NK cells and expansion of Th1 helper T cells and CTLs[12,13]. TLR9 agonists also promote maturation of B cells into plasma cells, thereby inducing a humoral immune response. Local tumor administration of CpG ODNs resulted in regression in distant tumors in murine cervical carcinoma models[14]. TLR9 agonists have also been shown to potentiate conventional anticancer therapies such as chemotherapy, radiation therapy and other immunotherapies[15,16]. As seen, TLR9 agonists uniquely orchestrate both innate and adaptive anti-tumor immune responses and may show synergistic therapeutic efficacy when used in combination with other immune adjuvants[17].

Binding of viral dsRNA and ATP in the cytoplasm to RIG-1 allows for association with adaptor protein IFN-beta promotor stimulator-1 (IPS-1) and subsequent production of type 1 IFN[18,19]. Melanoma differentiation-associated antigen 5 (MDA5) is highly homologous to RIG-1. Similarly, upon binding to dsRNA fragments, MDA5 initiates cytokine and type 1 IFN production through IPS-1 signaling[20–22]. This danger signaling pathway promotes anti-tumor immunity through activation of NK cells and CTLs and downregulation of Tregs[23–26] .

Tumor associated antigens and immune adjuvants are often nucleic acids that are unstable and highly susceptible to degradation by nucleases and proteases. Encapsulation in particles protects the contents from rapid degradation and enables modulation of delivery kinetics. The kinetics of antigen presentation plays a major role in determining the strength, duration, and memory phenotype of induced immune responses. Dose-escalating antigen contact resulted in much stronger CD8+ T cell responses compared to single administration of antigen[27]. This supports design of a slow release particle delivery system achievable using PLGA nanoparticles rather than a rapid burst release system that is characteristic of liposomal nanoparticles[28,29]. Co-encapsulating antigens and adjuvants in nanoparticles allows for more efficient uptake by phagocytic APCs and cross-presentation that promotes activation of anti-tumor CTLs and memory T cells[30–34].

C. METHODS

PLGA nanoparticle fabrication

First, make 10 mL stock solution of ethyl acetate and PLGA, 200mg/mL, place into cleaned scintillation vial. Then make appropriate stock solution of peptide in water (**not** PBS), 10-100mg/ml. Next, make up 100mL 1g/100mL of Mowiol 4-88 PVA in water (1%m/v). Pipette 1 mL of PLGA/ethyl acetate solution into 15mL plastic conical tube then pipette 50ul of stock protein (or water, in

control solution) into vial, place in ice bath. Place 15mL conical inside 50mL plastic conical, where the 50mL conical is filled with ice. Power setting for particles is target 7-8 W, which translates to approximately 30 on amplitude setting. Lower the sonicator probe into the solution and hit for (5s on, 10s off) x5 on ice. Add 2 mL of 1% stock PVA solution. Sonicate again in probe sonicator for (5s on, 10s off) x5 on ice. Using serological pipette gun, transfer contents to clean beaker, stir gently with small stir. Dropwise add to top (18mL or so) 1% PVA solution. Stir for 2-3 hours in fume hood to let ethyl acetate evaporate, should only very faintly or not smell of ethyl acetate any longer. Place entire contents into large falcon tube, spin down at 500rpm (on big centrifuge) for 10 minutes to pellet out large population (~5um) particles. Discard or keep this pellet you wish, but pipette off supernatant into new centrifuge tube. Spin down at 2500rpm for 10 min (up to 15 min) to pellet second population, ~500nm particles. Remove supernatant, these are tiny particles and excess PVA. Resuspend in minimal DI water using squeeze bottle to agitate the pellet, as it will be difficult to disperse. Then top up volume to 50mL with 1% PVA solution used above. If slightly higher yield is desired or pellet appears too small, take supernatant from 2500rpm centrifugation and run at 3500rpm for 10 minutes, supernatant from this centrifuge step should be completely discarded. Wash each centrifugation from each speed separately, 3x supernatant discarded each time. 2500 and 3500rpm can be

combined at this point. Then resuspend to 5mL in 1% PVA, ensure it is well dispersed.

Scanning Electron Microscopy

Nanoparticle PLGA were mounted on a flat SEM mount with colloidal graphite (Ted Pella). Samples were imaged by Carl Zeiss Ultra 55 Field Emission Scanning Electron Microscope using an in-lens secondary electron detector at San Francisco State University.

Cell Culture

T2 cell cultures with cultured in RPMI media overnight and coincubated with PLGA nanoparticles for 24 hours. 24 hours later, T2 cells were harvested from well, pelleted and then transferred into a coculture well containing Jurkat T cells expressing NY-ESO1 TCR transduced with a lentivirus. After overnight coculture of Jurkat and T2 cells, cells were harvested for analysis. Mouse B16F10 melanoma cells were cultured using RPMI media supplemented with 10% fetal bovine serum. Before tumor inoculation, cells were harvested and washed twice with PBS before being loaded into syringes and injected subcutaneously into B6 mice at 10^5 cells per 100uL per mouse.

Flow Cytometric Analysis

For flow-based analysis, cells were harvested from culture dishes and pelleted by centrifugation. Cells were washed in PBS and then immediately stained with directly conjugated antibodies. FITC-CD69 was purchased from Biolegend. Data analysis was performed with FlowJo software.

Mice

Female C57BL/6 mice aged 6-8 weeks were purchased from Jackson laboratories. Each mice was labeled with ear tag and inoculated subcutaneously with 10^5 B16F10 cells resuspended in serum free PBS buffer. Mice were then treated with drug starting 3 days after tumor inoculation for 4 doses separated 3 days apart. Drugs were delivered either intratumorally by injecting a total of 100uL of drug formula in 4 separate sites in the tumor. Intravenous injection was delivered through tail-vein by injecting a total of 200uL of drug per dose. Tumor measurements were performed using a caliper twice a week until animals expired.

D. RESULTS

Fabrication of Nanoparticle cancer vaccines

Tumor specific antigen gp100 and adjuvant cocktail consisting of STING, RIG-I, and TLR9 agonists are encapsulated within poly(lactic-co-glycolic acid) (PLGA) copolymer is fabricated using a double emulsion method. PLGA is first

dissolved in ethylene diacetate and antigen/adjuvant is resuspended in nuclease free water. PLGA organic fraction is added to the aqueous antigen/adjuvant fraction and sonicated on ice. Surfactant solution is then added to the first emulsion fraction and further sonicated on ice to form the second emulsion. The final double emulsified fraction is added dropwise to surfactant and stirred to evaporate off the ethyl acetate. Finally, particles are freeze dried for storage before use.

Characterization of the nanoparticles was performed by dynamic light scattering and scanning electron microscopy. Our results demonstrate that we were able to successfully fabricate homogenous PLGA nanoparticles measuring median diameter of 668 nm (**Fig 3.1**). In addition, scanning electron microscopy confirms the dimensions and morphology of these nanoparticles (**Fig 3.2**). The encapsulation efficiency of this protocol is 22.5% (data not shown), measured by measuring the total mass of peptide eluted out of the particles divided by the input mass of peptide. The particles can be thoroughly resuspended in saline and can readily pass through a 28 gauge needle without resistance.

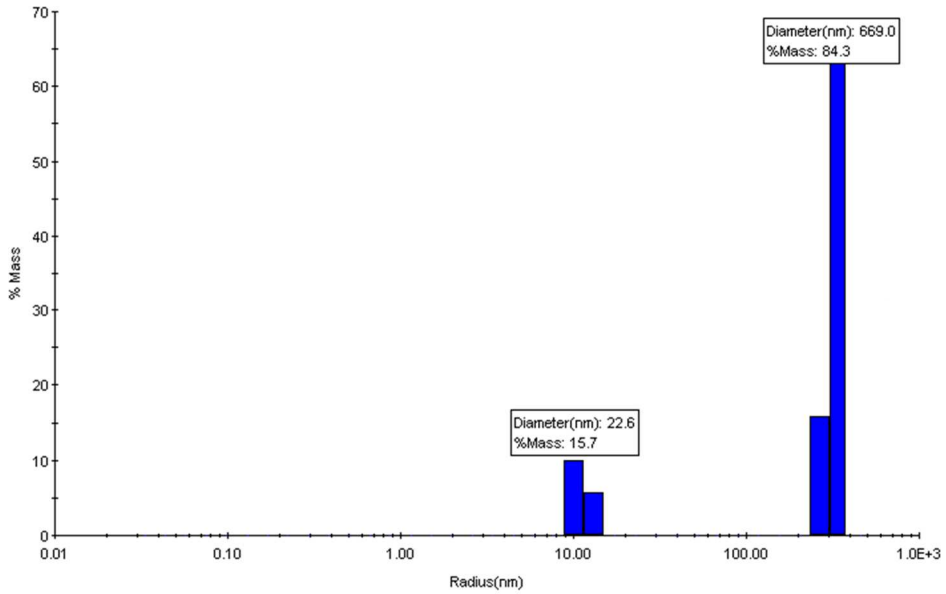

Figure 3.1 Dynamic light scattering data of fabricated antigen-adjuvant containing PLGA nanoparticles. Histogram plot of dynamic light scattering analysis of PLGA nanoparticles formulated by double emulsion system show a majority homogenous population of particles measuring 668 nm in diameter. A smaller population of particles measuring just 22.6 nm also exists but is a minority population representing just 15.7% of total particles.

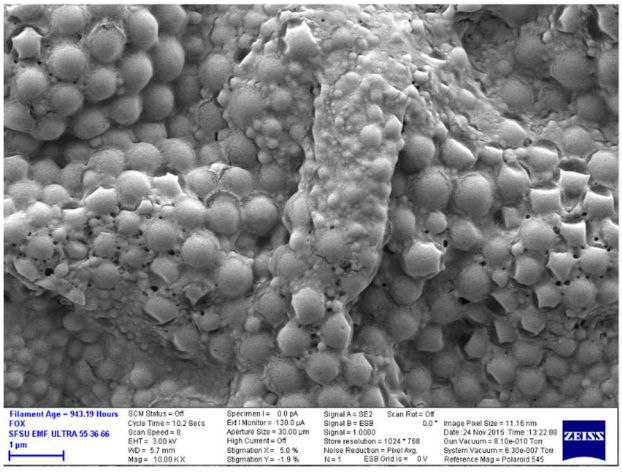

Figure 3.2 Scanning electron micrograph of fabricated antigen-adjuvant containing PLGA nanoparticles. Scanning electron micrograph of PLGA nanoparticles show uniform morphology or individual particles and majority particle diameter approximately 500nm. (scale bar = 1 micrometer)

Presentation of encapsulated antigen

We further assessed the efficacy of antigens encapsulated within PLGA nanoparticles to confirm that the structure of the peptide was not disrupted in the encapsulation process. Microparticles and nanoparticles encapsulating the NY-ESO1 peptide was fabricated using a similar double emulsion method as described above. The PLGA particles were cocultured for 24 hours with T2 antigen presenting cells to allow for antigen uptake and presentation. Jurkat T cells were transduced with a T Cell Receptor (TCR) specific to the NY-ESO1 peptide antigen and cocultured with the T2 cells. Following overnight coculture, flow cytometric analysis was performed on the jurkat T cells to assess their activation status via the CD69 activation surface marker (**Fig 3.3**). As negative controls, empty particles were cocultured with T2 cells and subjected to untransduced Tcells. The results of this study demonstrate that both PLGA microparticles and nanoparticles were able to successfully deliver NY-ESO-1 peptide antigen to T2 cells, and cause presentation of T2 cell surface. NY-ESO1 TCR specific Jurkat T cells showed increased expression of CD69

surface marker for cell activation when cocultured with peptide pulsed T2 APC. Negative controls containing empty particles did not result in expression of CD69 on Jurkat T cells. The results of this study give us confidence that the peptide antigens structures are preserved adequately during the double emulsion fabrication process such that they can still be delivered and presented by antigen presenting cells to activate antigen specific T cells in vitro.

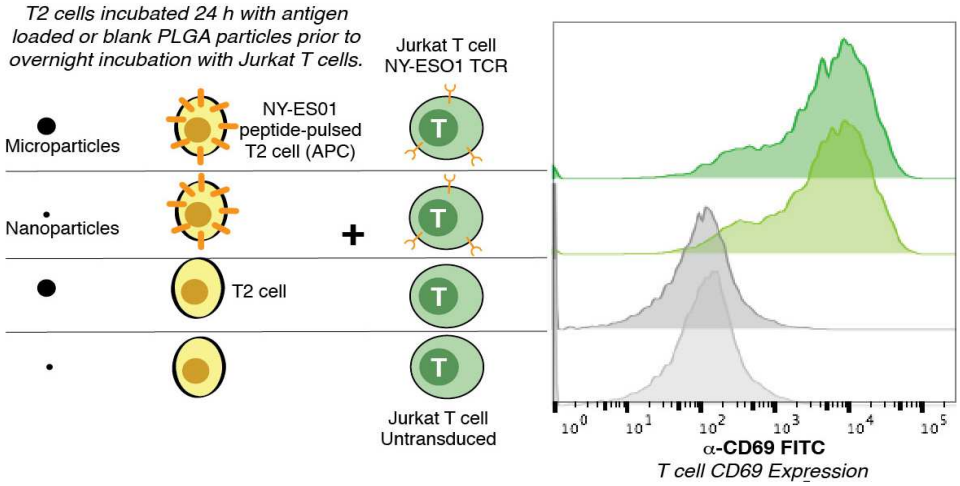

Figure 3.3 Antigen presentation of peptide loaded PLGA particles. NY-ESO-1 loaded PLGA particles by double emulsion method cocultured with T2 antigen presenting cells and Jurkat T cells transduced with NY-ESO1 specific T cell receptors illicit T cell activation measured by CD69 expression by flow cytometric analysis.

PLGA nanoparticles inhibit tumor growth in vivo

The efficacy of PLGA nanoparticle tumor vaccines were assessed using a syngeneic mouse model. 10^5 B16F10 melanoma cells were injected subcutaneously into wildtype female B6 mice. 3 days following tumor injections, the mice were treated with adjuvant-peptide loaded nanoparticles intravenously, or intratumorally, free adjuvant-peptide cocktail intravenously and intratumorally. As controls, empty nanoparticle vehicle and PBS were injected intratumorally in separate groups as well. Each animal was treated with 4 injections spaced 3 days apart. Tumor volumes were measured using a caliper at least once a week once the tumors become palpable.

In this preventative nanoparticle tumor vaccine model, we demonstrate that there was a detectable response in tumor bearing animals treated intratumorally with the adjuvant-peptide combination. Tumor volumes for mice treated with adjuvant-peptide cocktails and nanoparticles were significantly lower than those animals treated intratumorally with PBS or empty nanoparticle controls at day 26 after tumor inoculation. Although not statistically significant, animals treated with empty nanoparticles had tumor growths that were slightly greater than those treated with PBS. Naked adjuvant-peptide cocktail delivered intratumorally was slightly more potent, although not statistically significant compared to nanoparticle formulations of the adjuvant-peptide combination.

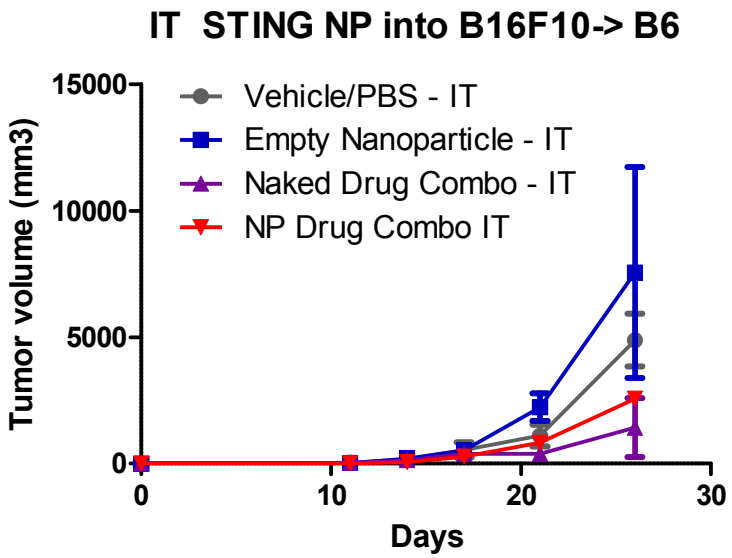

Figure 3.4 Intratumoral delivery of adjuvant-peptide loaded nanoparticle tumor vaccines. Wildtype B6 mice inoculated with 10^5 B16F10 melanoma cells were treated by intratumoral injection starting day 3 for 4 doses every 3 days with the corresponding drug and formulations. Tumor volumes were measured twice a week to assess antitumor response.

By delivering adjuvants and peptides directly into the tumor microenvironment, there is reduced chance of degradation of adjuvants. In this particular study, we show there was not a significant therapeutic benefit in formulating adjuvant-peptide cocktails within nanoparticles. Although intratumorally delivered vaccines is easy to administer and avoids the need for a nanoparticulate formulation, its utility may be limited by cutaneously accessible tumors such as melanoma, head and neck tumors, or breast tumors

in certain circumstances. In order to access other types of solid tumors, intravenous delivery of adjuvants and peptides may be necessary.

Again, using a preventative tumor vaccine model, we delivered the adjuvant-peptide cocktails intravenously. Each mouse received 10^5 B16F10 melanoma cells subcutaneously and received intravenous treatment of nanoparticle formulated or free adjuvant-peptide cocktail three days following tumor inoculation. Treatment continued every 3 days for up to 4 doses. Tumors on animals were measured once palpable using a caliper until animals expired. In this study, we show that compared to the PBS control treated animals, free adjuvant-peptide cocktails significantly reduced the rate of growth of melanoma tumors. Nevertheless, the anti-tumor efficacy observed in intravenous delivered adjuvant-peptide cocktail was not significantly improved compared to intratumural delivery. Nanoparticle formulation of adjuvant-peptide cocktail not only was more potent but actually significantly inhibited tumor growth past the treatment period. Tumor growth was not measurable throughout the duration of the study. These results strongly suggest therapeutic benefit in intravenous delivered nanoparticulate formulation of adjuvant-peptide combination. The benefit of PLGA nanoparticle formulation is more clearly observed in this intravenous delivery experiment as unencapsulated adjuvants are more likely to be degraded as they circulate before being delivered to a target.

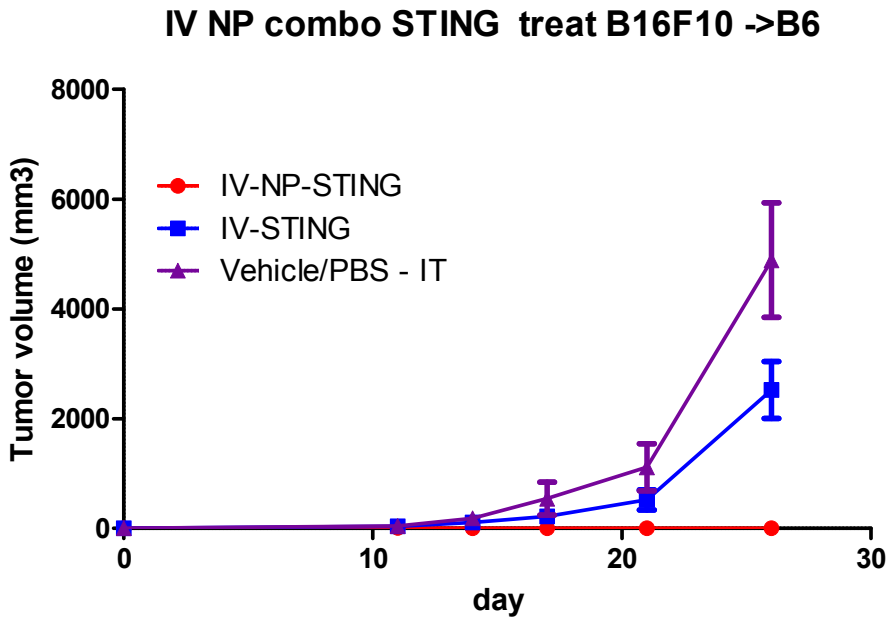

Figure 3.5 Intravenous delivery of adjuvant-peptide loaded nanoparticle tumor vaccines. Wildtype B6 mice inoculated with 10^5 B16F10 melanoma cells were treated by intravenous injection starting day 3 for 4 doses every 3 days with the corresponding drug and formulations. Tumor volumes were measured twice a week to assess antitumor response.

E. DISCUSSION

Oncolytic virus inspired nanoparticle tumor vaccines have the promise of achieving anti-tumor response in solid tumors. By employing a potent triple adjuvant cocktail consisting of RIG-I, STING, and TLR9 agonists, we demonstrate efficacy of this nanoparticle vaccine in a syngeneic mouse

melanoma model. We show that intravenous delivery route was more potent in achieving anti-tumor response compared with intratumorally delivered nanoparticles. This potency was not observed in adjuvant-peptides not protected by PLGA nanoparticles. Here, we show the ability of augment the potency of tumor vaccines and access tumors that cannot be reached cutaneously using a nanoparticle encapsulation system. When compared to oncolytic viruses, nanoparticle tumor vaccines are easier and cheaper to fabricate. Moreover, we show that multiple doses can be delivered intravenously to achieve therapeutic anti-tumor response.

Future studies investigating combination of nanoparticle formulated tumor vaccines with anti-PD-1 or anti-CTLA4 vaccines in other solid tumor types will be important. In particular, studying the ability these nanoparticles of turning 'cold' tumors that are resistant to immunotherapy into 'hot' tumors by looking at tumor infiltrating lymphocytes will be interesting as well.

F. REFERENCES

(1) Andtbacka, R. H. I.; Kaufman, H. L.; Collichio, F.; Amatruda, T.; Senzer, N.; Chesney, J.; Delman, K. A.; Spitler, L. E.; Puzanov, I.; Agarwala, S. S.; *et al.* Talimogene Laherparepvec Improves Durable Response Rate in Patients With Advanced Melanoma. *J. Clin. Oncol.* **2015**, *33*, 2780–2788.

(2) Lichty, B. D.; Breitbach, C. J.; Stojdl, D. F.; Bell, J. C. Going Viral with Cancer Immunotherapy. *Nat. Rev. Cancer* **2014**, *14*, 559–567.

(3) Zamarin, D.; Holmgaard, R. B.; Subudhi, S. K.; Park, J. S.; Mansour, M.; Palese, P.; Merghoub, T.; Wolchok, J. D.; Allison, J. P. Localized Oncolytic Virotherapy Overcomes Systemic Tumor Resistance to Immune Checkpoint Blockade Immunotherapy. *Sci. Transl. Med.* **2014**, *6*, 226ra32.

(4) Corrales, L.; Glickman, L. H.; McWhirter, S. M.; Kanne, D. B.; Sivick, K. E.; Katibah, G. E.; Woo, S.-R.; Lemmens, E.; Banda, T.; Leong, J. J.; *et al.* Direct Activation of STING in the Tumor Microenvironment Leads to Potent and Systemic Tumor Regression and Immunity. *Cell Rep.* **2015**, *11*, 1018–1030.

(5) Barber, G. N. STING: Infection, Inflammation and Cancer. *Nat. Rev. Immunol.* **2015**, *15*, 760–770.

(6) Woo, S.-R.; Fuertes, M. B.; Corrales, L.; Spranger, S.; Furdyna, M. J.; Leung,

M. Y. K.; Duggan, R.; Wang, Y.; Barber, G. N.; Fitzgerald, K. A.; *et al.* STING-Dependent Cytosolic DNA Sensing Mediates Innate Immune Recognition of Immunogenic Tumors. *Immunity* **2014**, *41*, 830–842.

(7) Deng, L.; Liang, H.; Xu, M.; Yang, X.; Burnette, B.; Arina, A.; Li, X.-D.; Mauceri, H.; Beckett, M.; Darga, T.; *et al.* STING-Dependent Cytosolic DNA Sensing Promotes Radiation-Induced Type I Interferon-Dependent Antitumor Immunity in Immunogenic Tumors. *Immunity* **2014**, *41*, 843–852.

(8) Fu, J.; Kanne, D. B.; Leong, M.; Glickman, L. H.; McWhirter, S. M.; Lemmens, E.; Mechette, K.; Leong, J. J.; Lauer, P.; Liu, W.; *et al.* STING Agonist Formulated Cancer Vaccines Can Cure Established Tumors Resistant to PD-1 Blockade. *Sci. Transl. Med.* **2015**, *7*, 283ra52.

(9) Hemmi, H.; Takeuchi, O.; Kawai, T.; Kaisho, T.; Sato, S.; Sanjo, H.; Matsumoto, M.; Hoshino, K.; Wagner, H.; Takeda, K.; *et al.* A Toll-like Receptor Recognizes Bacterial DNA. *Nature* **2000**, *408*, 740–745.

(10) Latz, E.; Verma, A.; Visintin, A.; Gong, M.; Sirois, C. M.; Klein, D. C. G.; Monks, B. G.; McKnight, C. J.; Lamphier, M. S.; Duprex, W. P.; *et al.* Ligand-Induced Conformational Changes Allosterically Activate Toll-like Receptor 9. *Nat. Immunol.* **2007**, *8*, 772–779.

(11) Iwasaki, A.; Medzhitov, R. Toll-like Receptor Control of the Adaptive Immune Responses. *Nat. Immunol.* **2004**, *5*, 987–995.

(12) Krieg, A. M. Toll-like Receptor 9 (TLR9) Agonists in the Treatment of Cancer. *Oncogene* **2008**, *27*, 161–167.

(13) Vollmer, J.; Weeratna, R.; Payette, P.; Jurk, M.; Schetter, C.; Laucht, M.; Wader, T.; Tluk, S.; Liu, M.; Davis, H. L.; *et al.* Characterization of Three CpG Oligodeoxynucleotide Classes with Distinct Immunostimulatory Activities. *Eur. J. Immunol.* **2004**, *34*, 251–262.

(14) Baines, J.; Celis, E. Immune-Mediated Tumor Regression Induced by CpG-Containing Oligodeoxynucleotides. *Clin. Cancer Res.* **2003**, *9*, 2693–2700.

(15) Weigel, B. J.; Cooley, S.; Defor, T.; Weisdorf, D. J.; Panoskaltsis-Mortari, A.; Chen, W.; Blazar, B. R.; Miller, J. S. Prolonged Subcutaneous Administration of 852A, a Novel Systemic Toll-like Receptor 7 Agonist, to Activate Innate Immune Responses in Patients with Advanced Hematologic Malignancies. *Am. J. Hematol.* **2012**, *87*, 953–956.

(16) Milas, L.; Mason, K. a; Ariga, H.; Hunter, N.; Neal, R.; Valdecanas, D.; Krieg, a M.; Whisnant, J. K. CpG Oligodeoxynucleotide Enhances Tumor Response to Radiation. *Cancer Res.* **2004**, *64*, 5074–5077.

(17) Klinman, D. M. Immunotherapeutic Uses of CpG Oligodeoxynucleotides. *Nat. Rev. Immunol.* **2004**, *4*, 249–259.

(18) Kawai, T.; Akira, S. Toll-like Receptor and RIG-1-like Receptor Signaling. *Ann. N. Y. Acad. Sci.* **2008**, *1143*, 1–20.

(19) Kato, H.; Sato, S.; Yoneyama, M.; Yamamoto, M.; Uematsu, S.; Matsui, K.; Tsujimura, T.; Takeda, K.; Fujita, T.; Takeuchi, O.; *et al.* Cell Type-Specific Involvement of RIG-I in Antiviral Response. *Immunity* **2005**, *23*, 19–28.

(20) Kang, D.-C.; Gopalkrishnan, R. V; Lin, L.; Randolph, A.; Valerie, K.; Pestka, S.; Fisher, P. B. Expression Analysis and Genomic Characterization of Human Melanoma Differentiation Associated Gene-5, Mda-5: A Novel Type I Interferon-Responsive Apoptosis-Inducing Gene. *Oncogene* **2004**, *23*, 1789–1800.

(21) Kato, H.; Takeuchi, O.; Sato, S.; Yoneyama, M.; Yamamoto, M.; Matsui, K.; Uematsu, S.; Jung, A.; Kawai, T.; Ishii, K. J.; *et al.* Differential Roles of MDA5 and RIG-I Helicases in the Recognition of RNA Viruses. *Nature* **2006**, *441*, 101–105.

(22) Kawai, T.; Takahashi, K.; Sato, S.; Coban, C.; Kumar, H.; Kato, H.; Ishii, K. J.; Takeuchi, O.; Akira, S. IPS-1, an Adaptor Triggering RIG-I- and Mda5-Mediated Type I Interferon Induction. *Nat Immunol* **2005**, *6*, 981–988.

(23) Kurooka, M.; Kaneda, Y. Inactivated Sendai Virus Particles Eradicate Tumors by Inducing Immune Responses through Blocking Regulatory T Cells. *Cancer Res.* **2007**, *67*, 227–236.

(24) Kaneda, Y. Virosome: A Novel Vector to Enable Multi-Modal Strategies for Cancer Therapy. *Adv. Drug Deliv. Rev.* **2012**, *64*, 730–738.

(25) Poeck, H.; Besch, R.; Maihoefer, C.; Renn, M.; Tormo, D.; Morskaya, S. S.; Kirschnek, S.; Gaffal, E.; Landsberg, J.; Hellmuth, J.; *et al.* 5'-Triphosphate-siRNA: Turning Gene Silencing and Rig-I Activation against Melanoma. *Nat. Med.* **2008**, *14*, 1256–1263.

(26) Besch, R.; Poeck, H.; Hohenauer, T.; Senft, D.; Häcker, G.; Berking, C.; Hornung, V.; Endres, S.; Ruzicka, T.; Rothenfusser, S.; *et al.* Proapoptotic Signaling Induced by RIG-I and MDA-5 Results in Type I Interferon-Independent Apoptosis in Human Melanoma Cells. *J. Clin. Invest.* **2009**, *119*, 2399–2411.

(27) Johansen, P.; Storni, T.; Rettig, L.; Qiu, Z.; Der-Sarkissian, A.; Smith, K. A.; Manolova, V.; Lang, K. S.; Senti, G.; Müllhaupt, B.; *et al.* Antigen Kinetics Determines Immune Reactivity. *Proc. Natl. Acad. Sci. U. S. A.* **2008**, *105*, 5189–5194.

(28) Demento, S. L.; Cui, W.; Criscione, J. M.; Stern, E.; Tulipan, J.; Kaech, S. M.; Fahmy, T. M. Role of Sustained Antigen Release from Nanoparticle Vaccines in Shaping the T Cell Memory Phenotype. *Biomaterials* **2012**, *33*, 4957–4964.

(29) Moon, J. J.; Suh, H.; Bershteyn, A.; Stephan, M. T.; Liu, H.; Huang, B.; Sohail, M.; Luo, S.; Um, S. H.; Khant, H.; *et al.* Interbilayer-Crosslinked Multilamellar Vesicles as Synthetic Vaccines for Potent Humoral and Cellular Immune Responses. *Nat. Mater.* **2011**, *10*, 243–251.

(30) Mukai, Y.; Yoshinaga, T.; Yoshikawa, M.; Matsuo, K.; Yoshikawa, T.; Matsuo, K.; Niki, K.; Yoshioka, Y.; Okada, N.; Nakagawa, S. Induction of Endoplasmic Reticulum-Endosome Fusion for Antigen Cross-Presentation Induced by Poly (-Glutamic Acid) Nanoparticles. *J. Immunol.* **2011**, *187*, 6249–6255.

(31) Stano, A.; Scott, E. A.; Dane, K. Y.; Swartz, M. A.; Hubbell, J. A. Tunable T Cell Immunity towards a Protein Antigen Using Polymersomes vs. Solid-Core Nanoparticles. *Biomaterials* **2013**, *34*, 4339–4346.

(32) Blander, J. M.; Medzhitov, R. Toll-Dependent Selection of Microbial Antigens for Presentation by Dendritic Cells. *Nature* **2006**, *440*, 808–812.

(33) Schlosser, E.; Mueller, M.; Fischer, S.; Basta, S.; Busch, D. H.; Gander, B.; Groettrup, M. TLR Ligands and Antigen Need to Be Coencapsulated into the Same Biodegradable Microsphere for the Generation of Potent Cytotoxic T Lymphocyte Responses. *Vaccine* **2008**, *26*, 1626–1637.

(34) Zaks, K.; Jordan, M.; Guth, A.; Sellins, K.; Kedl, R.; Izzo, A.; Bosio, C.; Dow, S. Efficient Immunization and Cross-Priming by Vaccine Adjuvants Containing TLR3 or TLR9 Agonists Complexed to Cationic Liposomes. *J. Immunol.* **2006**, *176*, 7335–7345.

Publishing Agreement

It is the policy of the University to encourage the distribution of all theses, dissertations, and manuscripts. Copies of all UCSF theses, dissertations, and manuscripts will be routed to the library via the Graduate Division. The library will make all theses, dissertations, and manuscripts accessible to the public and will preserve these to the best of their abilities, in perpetuity.

Please sign the following statement:

I hereby grant permission to the Graduate Division of the University of California, San Francisco to release copies of my thesis, dissertation, or manuscript to the Campus Library to provide access and preservation, in whole or in part, in perpetuity.

3-11-17

Author Signature | Date